






A novel high-volume Photochemical Emission Aging flow tube Reactor (PEAR)

Mika Ihalainen, Petri Tiitta, Hendryk Czech, Pasi Yli-Pirilä, Anni Hartikainen, Miika Kortelainen, Jarkko Tissari, Benjamin Stengel, Martin Sklorz, Heikki Suhonen, Heikki Lamberg, Ari Leskinen, Astrid Kiendler-Scharr, Horst Harndorf, Ralf Zimmermann, Jorma Jokiniemi & Olli Sippula


To cite this article: Mika Ihalainen, Petri Tiitta, Hendryk Czech, Pasi Yli-Pirilä, Anni Hartikainen, Miika Kortelainen, Jarkko Tissari, Benjamin Stengel, Martin Sklorz, Heikki Suhonen, Heikki Lamberg, Ari Leskinen, Astrid Kiendler-Scharr, Horst Harndorf, Ralf Zimmermann, Jorma Jokiniemi & Olli Sippula (2019) A novel high-volume Photochemical Emission Aging flow tube Reactor (PEAR), *Aerosol Science and Technology*, 53:3, 276-294, DOI: [10.1080/02786826.2018.1559918](https://doi.org/10.1080/02786826.2018.1559918)

To link to this article: <https://doi.org/10.1080/02786826.2018.1559918>

 View supplementary material 


 Published online: 17 Jan 2019.

 Submit your article to this journal 

 Article views: 480

 View related articles 

 View Crossmark data 

 Citing articles: 13 View citing articles 



A novel high-volume Photochemical Emission Aging flow tube Reactor (PEAR)

Mika Ihalainen^a, Petri Tiitta^a, Hendryk Czech^a, Pasi Yli-Pirilä^a, Anni Hartikainen^a, Miika Kortelainen^a, Jarkko Tissari^a, Benjamin Stengel^b, Martin Sklorz^{c,d}, Heikki Suhonen^a, Heikki Lamberg^a, Ari Leskinen^{e,f}, Astrid Kiendler-Scharr^g, Horst Harndorf^b, Ralf Zimmermann^{c,d}, Jorma Jokiniemi^a, and Olli Sippula^{a,h}

^aFine Particle & Aerosol Technology Laboratory, Department of Environmental and Biological Science, University of Eastern Finland, Kuopio, Finland; ^bChair of Piston Machines and Internal Combustion Engines, Faculty of Mechanical Engineering and Marine Technology, University of Rostock, Rostock, Germany; ^cJoint Mass Spectrometry Centre, Chair of Analytical Chemistry, University of Rostock, Rostock, Germany; ^dJoint Mass Spectrometry Centre, Cooperation Group “Comprehensive Molecular Analytics”, Helmholtz Zentrum München, Neuherberg, Germany; ^eFinnish Meteorological Institute, Kuopio, Finland; ^fAtmospheric Aerosol Physics, Department of Applied Physics, University of Eastern Finland, Kuopio, Finland; ^gForschungszentrum Jülich, Institute for Energy and Climate Research IEK-8: Troposphere, Jülich, Germany; ^hDepartment of Chemistry, University of Eastern Finland, Joensuu, Finland

ABSTRACT

Aerosols emitted from various anthropogenic and natural sources undergo constant physicochemical transformations in the atmosphere, altering their impacts on health and climate. This article presents the design and characteristics of a novel Photochemical Emission Aging flow tube Reactor (PEAR). The PEAR was designed to provide sufficient aerosol mass and flow for simultaneous measurement of the physicochemical properties of aged aerosols and emission exposure studies (*in vivo* and *in vitro*). The performance of the PEAR was evaluated by using common precursors of secondary aerosols as well as combustion emissions from a wood stove and a gasoline engine. The PEAR was found to provide a near laminar flow profile, negligible particle losses for particle sizes above 40 nm, and a narrow residence time distribution. These characteristics enable resolution of temporal emission patterns from dynamic emission sources such as small-scale wood combustion. The formation of secondary organic aerosols (SOA) in the PEAR was found to be similar to SOA formation in a smog chamber when toluene and logwood combustion emissions were used as aerosol sources. The aerosol mass spectra obtained from the PEAR and smog-chamber were highly similar when wood combustion was used as the emission source. In conclusion, the PEAR was found to plausibly simulate the photochemical aging of organic aerosols with high flow rates, needed for studies to investigate the effects of aged aerosols on human health. The method also enables to study the aging of different emission phases in high time resolution, and with different OH-radical exposures up to conditions representing long-range transported aerosols.

ARTICLE HISTORY

Received 1 August 2018
Accepted 27 November 2018

EDITOR

Matti Maricq

1. Introduction

Atmospheric aerosols have direct and indirect effects on climate (Myhre et al. 2009; Pöschl 2005; Ramanathan et al. 1989). Furthermore, airborne particulates with an aerodynamic diameter below 2.5 μm ($\text{PM}_{2.5}$) have been associated with negative impacts on human health in epidemiological and toxicological studies (Happo et al. 2014; Laden et al. 2000; Maier et al. 2008; Pope et al. 2004). The sources of atmospheric aerosols can be of natural or anthropogenic origin, however natural sources account for the majority of atmospheric aerosol mass (Boucher 2015).

Despite this, the contribution of anthropogenic aerosols to the total ambient $\text{PM}_{2.5}$ concentration can be substantial, particularly within urban areas where there is a concentration of traffic, industry, and energy production. Physicochemical properties of primary emissions undergo rapid changes as soon as they are emitted into atmosphere, through reactions with atmospheric oxidizing agents, such as OH, O_3 , and NO_3 radicals (Atkinson and Arey 2003), and changes in aerosol dynamics, including coagulation/agglomeration and partitioning between gas- and particle phases (Asa-Awuku et al. 2009). The oxidation of

CONTACT Olli Sippula olli.sippula@uef.fi Fine Particle & Aerosol Technology Laboratory, Department of Environmental and Biological Science, University of Eastern Finland, Yliopistonranta 1, P.O. Box 1627, Kuopio FI-70211, Finland.

Color versions of one or more of the figures in the article can be found online at www.tandfonline.com/uast.

Supplemental data for this article can be accessed on the [publisher's website](#).

organic vapors and inorganic gases, such as NO_x and SO_2 , leads to the formation of secondary organic aerosols (SOA) and inorganic aerosols, which are linked to the majority of ambient aerosols (Jimenez et al. 2009) and can increase ambient PM mass concentrations many times over (Huang et al. 2014). Additionally, heterogeneous oxidation alters the chemical composition of primary organic aerosol (POA), forming aged POA (Kroll et al. 2015). Currently, one of the main challenges for the assessment of the environmental impacts of anthropogenic aerosol emissions is understanding their transformation in the atmosphere, which changes the chemical, physical, and health-related properties of the emissions.

Previous investigators have studied the mechanisms of SOA formation and the impact of aerosol aging on physicochemical properties of aerosol particles, using different emission sources and single precursors, and both batch (Chirico et al. 2010; Chu et al. 2017; Tiitta et al. 2016) and flow reactors (Ahlberg et al. 2017; Jathar et al. 2017; Ortega et al. 2013). Batch reactors and flow reactors are hereafter referred to as “smog chambers” and oxidation flow reactors” (OFR) respectively.

Smog chambers often consist of a Teflon bag surrounded by ultraviolet (UV) lamps or are made of metal with UV lamps placed inside. These systems are typically used to simulate either photochemical or dark ageing reactions at atmospherically relevant conditions and with chamber residence times of the order of a few hours to days. They are important tools for atmospheric scientists in elucidating the effects of various anthropogenic and natural emissions sources in the atmosphere. However, oxidant exposures in smog chambers are usually limited to maximum few days of equivalent photochemical age, due to the limited experiment time and the usage of atmospherically relevant oxidant concentrations. As a result, for example average carbon oxidation states (OS_C) of organic aerosols are typically lower in smog chamber-aged aerosols than in long-range transported aerosols (Ng et al. 2010) and the potential total aerosol mass (Kang, Root, and Brune 2007) may not be formed within the reactions simulated in the smog chambers. Furthermore, smog chambers are not able to address SOA formation potentials for changing molecular compositions of organic vapors during dynamic emissions, such as car emissions during driving cycles (Gullett, Oudejans, and Touati 2013) or batchwise logwood combustion (Czech et al. 2016), and are usually stationary and therefore inappropriate for experiments at different locations.

Mobile OFR typically have shorter residence times than smog chambers, of the order of seconds to minutes (Ezell et al. 2014; George et al. 2007; Kang, Root, and Brune 2007; Keller and Burtscher 2017; Simonen et al. 2017), and also allow field studies (Palm et al. 2016; Tkacik et al. 2014). Short residence times in combination with much higher exposures of atmospheric oxidizing agents enable oxidation reactions equivalent up to weeks of atmospheric aging, but may in theory result in different oxidation regimes than in the atmosphere. Moreover, they may lead to high saturation ratios of condensable vapors, and into a dominating nucleation mode for particles leaving an OFR (Keller and Burtscher 2017). However, the few comparisons between OFR and smog chambers so far have found that both methods provide similar OS_C and SOA yields at equal photochemical aging times (Bruns et al. 2015; Lambe et al. 2015). Nevertheless, all laboratory aging reactors provide imperfect simulations of atmospheric transformation processes and therefore utilizing of different designs of reactors, in addition to direct ambient measurements, are needed to form a complete picture of atmospheric processes.

Recent epidemiological and toxicological studies have indicated that both primary and secondary aerosols induce adverse effects on human health (Delfino et al. 2010; Huang et al. 2012; Shiraiwa et al. 2017; Verma et al. 2009). To study the role of atmospheric aging on the toxicological properties of aerosol emissions from a single source, relatively high aerosol sample volumes and concentrations are needed. Modern air–liquid interface cell exposure systems (Paur et al. 2011) require several cubic meters of sample per hour (Kanashova et al. 2018; Oeder et al. 2015) when combined with filter sampling and online physicochemical characterization of aerosols. This requirement can potentially be met with existing OFR methods (Ezell et al. 2010), but not without compromising the time resolution of the measurements. In a previous study using a smog chamber, the issue of low aerosol concentration has been tackled by aerosol enrichment (Künzi et al. 2015), but the effect of the enrichment technique on aerosol properties has not yet been clarified.

In this article, we propose a new high-volume oxidation flow reactor for emission aging studies, called “Photochemical Emission Aging flow tube Reactor” (PEAR) which aims to fulfill the following criteria: (1) Flow rate in the range of 50–200 L min^{-1} to provide sufficiently high flow rates for emission studies combining toxicological *in vitro/in vivo* studies with physicochemical characterization of emission aerosols; (2)

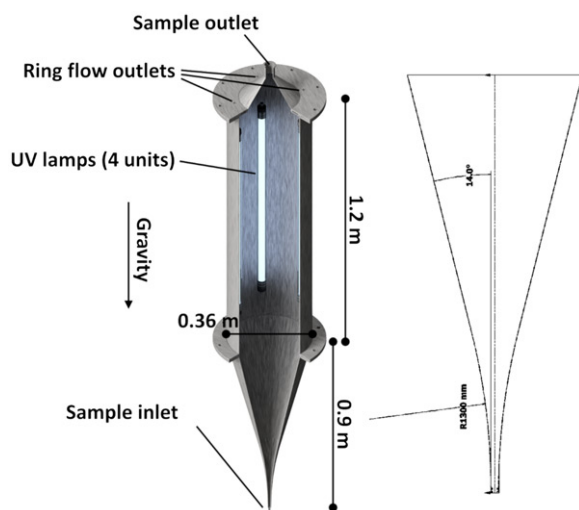


Figure 1. Geometry of the Photochemical Emission Aging flow tube reactor (PEAR; left) and geometry of the diffuser (right).

Adjustable and broad range of OH-radical concentrations similar to PAM-type OFR (Kang, Root, and Brune 2007), giving a possibility to photochemically age relatively high aerosol concentrations, and up to OH exposures representing long-range transported emissions (i.e. 1–10 days of photochemical age); (3) Independent control of OH and O₃ exposure, to simulate different oxidative conditions; and (4) Laminar flow profile with narrow residence time distribution (RTD) to provide photochemical processing with low interaction of sample with reactor walls, low wall losses and to enable distinction of highly time-dependent transient phases of emissions from combustion processes.

2. Methods

2.1. Photochemical Emission Aging flow tube Reactor (PEAR) setup

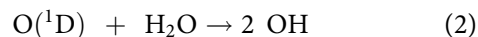
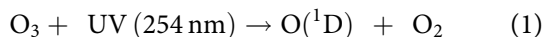
PEAR denotes an OFR with a total volume of 139 L, a total surface area of 2.28 m² and a resulting surface-to-volume ratio of 16.4 m⁻¹, including the surface area of the UV lamps. It consists of three sections with distinctive functions: the inlet diffuser, the reactor, and the outlet. All three sections are made mainly of (conductive) stainless steel (grade 316L) to avoid losses of charged particles (Brockmann 2001) and to enable easy cleaning. The inlet diffuser introduces the aerosol into the reactor. It was designed to minimize backflow and recirculation of the aerosol, which can occur as a result of an expanding cross-sectional area. It was constructed with the following dimensions: 90 cm length, 1 cm inner diameter (ID) at the inlet, and 36 cm ID at the outlet. For the design of

the PEAR inlet, we did not resort to conventional shallow angle cone (e.g. 7° half opening angle), since this would have made the diffuser unacceptably long (approx. 150 cm). Furthermore, it has been shown that the optimal opening angle depends on several parameters, e.g. flow Reynolds number at the diffuser inlet (Sparrow, Abraham, and Minkowycz 2009). Instead, the expansion profile of the diffuser follows a curvature of circular geometry ($R = 1300$ mm) until opening half angle of 14° is reached. Behind, the diffuser continues as a cone (Figure 1). The selection of this basic design is supported by numerical simulations (Section 2.2), which was also included for refining the geometry.

In the cylindrical reactor part, with 120 cm length and 36 cm inner diameter, four UV lamps (Osram, HNS 55W G13 HO) are located close to the inner wall of the reactor. The UV lights are surrounded by a quartz tube, which enables a flow of cooling air between the UV lamps and the quartz tubes. Cooling reduces temperature increase that would affect gas-particle partitioning and decreases relative humidity. As characteristic for mercury vapor lamps, the emission spectrum peaks at 254 nm and covers increasing emissions bands from UV-B up to visible blue light at approximately 440 nm (online Supplemental Information, Figure S1). Moreover, the UV lamps may be turned on and off individually and regulated to emit at various intensities.

The PEAR outlet has been divided into two concentric areas: the ring flow (4 cm wide circular outlet region near the wall) and the main sample flow. A small portion of the total flow (20%) is diverted to the ring flow outlet, which removes the near wall portion of the volume flow. Thus, wall losses and reactions of the measured aerosol are potentially reduced.

The photo-oxidation of the sample in the reactor follows the “Potential Aerosol Mass (PAM)” concept (Kang, Root, and Brune 2007; Lambe et al. 2011). OH radicals are produced inside the reactor by ozone (O₃) photolysis and subsequent reaction of the short-lived oxygen radical O(¹D) with water (H₂O) vapor through the following reactions:



The required ozone and water vapor are fed into the reactor externally and are pre-mixed with the aerosol sample before entering the PEAR. To minimize particle contamination, which might act as seed aerosol, the ozone–air mixture is filtered by a HEPA filter prior to introducing it to the main flow. Ozone

is generated by exposing purified air (Model 737–250, Aadco Instruments Inc., USA) or oxygen to a high-energy UV lamp (emission peak at 185 nm). The concentration of ozone at the PEAR outlet is measured with an ozone analyzer (Thermo 49i). The volumetric flow rate from the ozone generator outlet negligibly dilutes the aerosol sample by approximately 1% for a total flow of 100 L min^{-1} . The water vapor is produced from deionized water and from clean air which has been treated with an Aadco air purifier. Subsequently, the purified air of high humidity flows through a NafionTM humidifier (Perma Pure LLC, NJ, USA). The humidifier was heated to enhance the concentration of water vapor. The humidity of air has a substantial impact on aging chemistry and gas-particle partitioning (Jia and Xu 2013). If not otherwise stated, aging experiments were performed at $50 \pm 2\%$ relative humidity, which closely resembles ambient conditions, and with a volume flow rate at the humidifier outlet of less than 10% of the total aerosol flow. The relative humidity was measured and controlled using a humidity and temperature sensor (HMP 110/65, Vaisala, Finland) downstream of the PEAR.

The photon flux of lamps for the highest UV intensity was estimated as $1.8 \times 10^{16} \text{ photons cm}^{-2} \text{ s}^{-1}$, based on the known lamp power ($4 \times 55 \text{ W}$), lamp efficiency ($\sim 30\%$) and PEAR internal surface area (0.47 m^2). The validity of the calculated photon flux was checked by measuring the decay of O_3 due to photolysis. Based on the ozone decay, an estimate for maximum photon flux of $2.3 \times 10^{16} \text{ photons cm}^{-2} \text{ s}^{-1}$ is received using the Oxidation Flow Reactor Exposure Estimator 3.1 (Li et al. 2015; Peng et al., 2016), which is in good agreement with the lamp power-based estimate.

2.2. Design optimization by CFD simulation

Numerical simulations were applied during the design process of the PEAR with emphasis on the performance of the diffuser introducing aerosol sample into the reactor. Diffuser geometry was optimized by altering the geometry parameters (opening curvature radius and opening angle in Figure 1) and by observing the undesired backflow regions with numerical simulations. The average flow field was simulated using ANSYS Fluent (ANSYS 16.0) software in three dimensions. Turbulence was modeled using a SST-k-w-turbulence transfer model with advanced wall treatment. This model shows good performance among the turbulence models used for Reynolds-averaged Navier-Stokes (RANS) equations in diffuser-type CFD (Computational Fluid Dynamics) problems (El-Behery

and Hamed 2009; Obi, Aoki, and Masuda Kyoto, Japan, 1993). Nonetheless, Obi, Aoki, and Masuda (1993) demonstrated that the SST-k-w model may overpredict the extent of the separation region. Hybrid tetrahedral-hexahedral mesh consisting of 3.2 M computation cells were used. The steady state of the flow field was simulated. Simulation data was also applied to define the RTDs, as described in the next section.

2.3. Residence time distributions

A step input method was applied to experimentally evaluate the RTD. Downstream of the PEAR, mass flow controllers (suction) were used to set the desired flow rate into the tube while feeding purified air into the inlet. Two different flow rates of 50 (40 L min^{-1} main flow and 10 L min^{-1} side flow) and 100 L min^{-1} (80 L min^{-1} main flow and 20 L min^{-1} side flow) were used. The latter value was the optimal flow rate setting. After the flows were configured, a constant flow rate of CO_2 was injected into the flow tube inlet. The concentration of CO_2 was then monitored at the outlet of the PEAR with a trace level CO_2 analyzer (ABB AO2040). Measured CO_2 concentrations were smoothed by averaging the values with a moving time window of 5 s. Finally, the RTD was calculated from the differential CO_2 concentration at the outlet.

To compare the theoretical residence time results with the empirical ones, the progression of CO_2 gas in PEAR was simulated. Steady state results of the RANS flow fields were applied and only the progression of the CO_2 was solved as unsteady (e.g. Adeosun and Lawal 2009). Finally, the residence time function was solved by applying step input injection.

2.4. Particle losses

The particle losses in the flow tube were examined with silver aerosol particles. The silver aerosol particles were generated by spray pyrolysis. A liquid solution of AgNO_3 in methanol was atomized with an ultrasonic nebulizer (Pyrosol 7901, RBI, France). The atomized solution was transported with nitrogen gas (1.5 L min^{-1}) to a hot wall reactor (800°C). In the reactor the methanol evaporated and the AgNO_3 decomposed, forming metallic Ag particles. The products from the hot wall reactor were diluted in room temperature air (15 L min^{-1}) using a porous tube diluter. To investigate the relationship between particle loss and particle size, the generated particles were size classified with a differential mobility analyzer (DMA model 3081) operated with a sheath flow of

10 L min⁻¹, a sample flow of 3 L min⁻¹, and with electrical mobility sizes ranging from 20 to 200 nm. The aerosol fed to the PEAR was characterized with a scanning mobility particle sizer (SMPS, DMA model 3081 with sheath flow 3 L min⁻¹, CPC model 3775 with 0.3 L min⁻¹ sample flow, TSI Inc., Shoreview, MN, USA) upstream and after passing the PEAR. The same SMPS was used to measure particle number size distributions both up- and downstream of the PEAR to prevent systematic errors from occurring as a result of measuring with different devices. For each particle size, the stability of the silver particle generation and particle size distribution were monitored by measuring the upstream size distribution again after the downstream scans. At least three scans were measured for each condition.

2.5. Low-volatile organic compound (LVOC) losses

In the atmosphere organic compounds with low volatilities (LVOCs) typically condense onto aerosol particles. However, in flow reactors the loss of LVOCs can potentially be governed by other mechanisms (e.g. deposition onto chamber walls) due to the short aerosol residence times (Kang, Root, and Brune 2007; Lambe et al. 2011) and high concentration of oxidant in flow reactors (Palm et al. 2016). In the case that other mechanisms play a significant role in LVOC losses then the flow reactor measurements may underestimate the potential for SOA formation. To reduce wall losses, the PEAR was designed with a relatively small surface area to volume (A/V) ratio (16.4 m⁻¹). This value is lower than that of many smaller OFRs which have similar aerosol residence times (Ezell et al. 2010; George et al. 2007; Simonen et al. 2017) with the PEAR.

The lifetime for LVOC condensation onto aerosols with a diameter d_p at temperature T is calculated as

$$\tau = \frac{1}{\text{CS}} \quad (3)$$

where condensation sink (CS) with unit s⁻¹ is calculated as

$$\text{CS} = 2\pi D \int_0^\infty d_p \beta_M(d_p) n(d_p) dd_p \quad (4)$$

(Lehtinen et al. 2003) with the diffusion coefficient D and particle size distribution $n(d_p)$. The transitional correction factor β_M can be expressed as (Fuchs and Sutugin 1971)

$$\beta_M = \frac{Kn + 1}{0.377Kn + 1 + \frac{4}{3}\alpha^{-1}Kn^2 + \frac{4}{3}\alpha^{-1}Kn} \quad (5)$$

by using the accommodation coefficient α and the Knudsen number Kn . The latter can be calculated as

$$Kn = \frac{2\lambda_g}{d_p} \quad (6)$$

where λ_g is the mean free path of the condensing gas.

Similar to Palm et al. (2016), molecular mass M_g of 200 g mol⁻¹ for LVOCs, diffusion coefficient D of 7×10^{-6} m²s⁻¹ and accommodation coefficient α of 1 was applied.

Based on the simple LVOC model reported in Palm et al. (2016), and in the absence of condensation sink or oxidants, LVOC wall losses for PEAR flow tube are 8, 12, and 15% for residence times of 50, 75, and 100 s, respectively (online Supplemental Information). In all of the experiments with real combustion exhaust aerosols, the CS of aerosols was relatively high (minimum of 0.07 s⁻¹) and hence the condensation onto aerosols dominated the molecular flux of LVOC; the wall losses are estimated to be less than 2.1% for all different experiments and OH exposure cases. A more detailed description of the LVOC loss calculations can be found from the online Supplemental Information.

2.6. Determination of OH exposure by measuring SO₂ decay

The correlations between OH-radical concentrations, UV lamp voltage, relative humidity (HMP 110/65, Vaisala, Finland), and ozone feed (Thermo 49i) were investigated by measuring the decay of SO₂ (Thermo 43i-TLE) to sulfate aerosol during oxidation in the reactor. SO₂ was first fed into the reactor with purified air, ozone, and water vapor. The initial concentration of SO₂ in the reactor was 50 ppb. The rate of conversion of SO₂ was determined by measuring the SO₂ concentration up- and downstream of the PEAR at steady-state conditions, and applying the following pseudo-first order kinetic equation (Lambe et al. 2015):

$$\text{OH exposure} = -\frac{1}{k_{\text{SO}_2}^{\text{OH}}} \ln \left(\frac{[\text{SO}_2]}{[\text{SO}_2]_0} \right) \quad (7)$$

with a bimolecular kinetic constant k of 9×10^{-13} cm³ molec⁻¹ s⁻¹ (Davis, Ravishankara, and Fischer 1979).

2.7. Photochemical aging of toluene

Toluene is a SOA precursor compound, which is frequently used in aerosol aging experiments. Experiments were carried out with toluene to compare features of PEAR with those of previously reported OFR. Toluene vapor was fed into the PEAR without seed aerosol via a diffusion tube at initial concentrations of 94 and 230 ppb, together with ozone, purified air, and water vapor

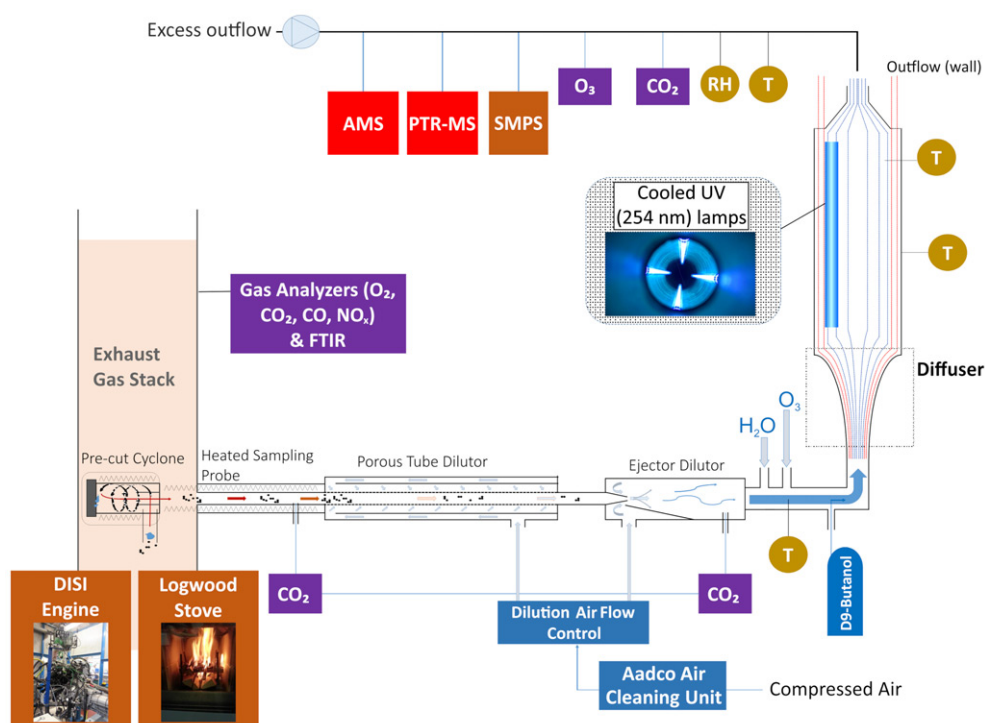


Figure 2. Schematic diagram of the experimental setup used for aging of combustion emission sources.

(relative humidity of 50%). The particles measured downstream of the reactor resulted from nucleation and subsequent condensation of oxidation products of the toluene. Toluene gas phase concentrations and particulate organic mass at the outflow of the PEAR were analyzed by a high-resolution proton-transfer-reaction time-of-flight mass spectrometer (HR-PTR-ToF-MS, Ionicon, Austria) and a high-resolution aerosol mass spectrometer (HR-AMS, Aerodyne Research Inc., MA, USA), respectively. The photochemical age of the resulting OA was estimated from a reaction constant between toluene and OH of $5.7 \times 10^{-12} \text{ cm}^3 \text{ s}^{-1}$ (Barmet et al. 2012), while SOA yields were calculated by dividing the formed OA mass by the reacted mass of toluene (Odum et al. 1996). OA from aging of toluene, as well as from the combustion emissions from sources described in the following section, were characterized from AMS mass spectra using the fragmentation table for elemental analysis of OA AMS spectra (Canagaratna et al. 2015) and OS_C calculation (Kroll et al. 2011).

2.8. Photochemical aging of real-world emission sources

The utilization of PEAR was demonstrated with emissions from two real-world emission sources to investigate its capability to simulate aging of complicated combustion aerosol mixtures, to follow sources with

dynamic emission profiles, and to determine SOA emission factors (EF).

In the first experiments, aging of emissions from a 2.0 L turbo-charged flexi-fuel direct injection spark-ignition engine (DISI) on an engine test bench were investigated using a PEAR flow rate of 50 L min^{-1} . The engine refers to a standard compact passenger car engine, equipped with a three-way catalyst and fulfilling the EURO5 emission norm. Commercial E10 gasoline, consisting of gasoline and maximum 10% bioethanol, was used as fuel. The engine was operated under conditions based on New European Driving Cycle (NEDC) as well as steady state conditions, corresponding to speeds of 80 and 120 km h^{-1} , which were controlled by an electric eddy current dynamometer (WM 400, Schenck RoTec GmbH, Germany). The presented engine cycle data comprises of emissions from NEDC-related engine power under hot start conditions (started after one cold start cycle), which was consecutively repeated four times. In the following sections, we refer to the NEDC-related driving conditions as “engine cycle” (EC) to avoid ambiguity error with emissions from true NEDC chassis dynamometer tests.

Engine emissions were first diluted with a dilution ratio of 40 by a combination of porous tube and ejector dilutors (Lyyrinen et al. 2004) (Vencontra, DAS, Finland). The diluted emissions were then

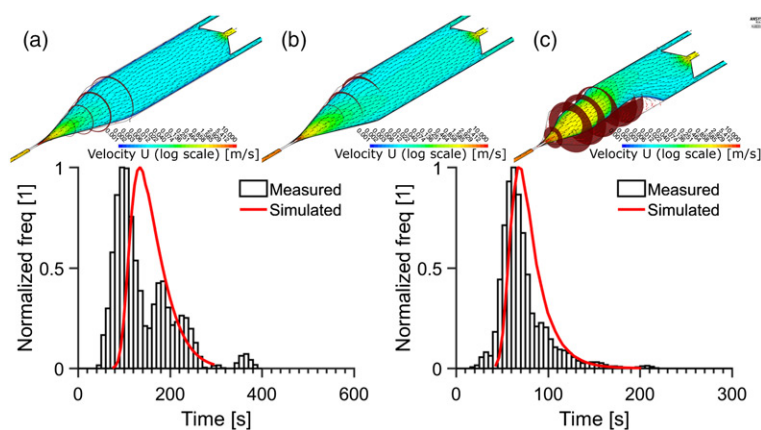


Figure 3. Top: Axial velocity fields from CFD simulations for optimized diffuser at flowrates (a) 50 L min^{-1} , (b) 100 L min^{-1} , and (c) a velocity field of a diffuser with too fast expansion diffuser design at 100 L min^{-1} , causing excessive back flows in comparison to a and b. Red circular areas show the regions where the axial flow direction is backwards. Bottom: residence time distributions for 50 L min^{-1} (left) and 100 L min^{-1} (right) flow rates.

premixed with water vapor and ozone, and finally introduced to the PEAR (Figure 2). OH exposure was estimated by continuously supplying a trace level of d9-butanol to the aerosol sample and subsequently measuring the decay of d9-butanol (Barmet et al. 2012) by a PTR quadrupole mass spectrometer (PTR-QMS, Ionicon, Austria). From the relative decay, OH exposure and related photochemical age was calculated assuming a reaction constant for d9-butanol and OH of $3.4 \times 10^{-12} \text{ cm}^3 \text{ s}^{-1}$ (Barmet et al. 2012). CO_2 concentrations were measured from the undiluted exhaust (FTIR, Gaset, Finland and AIDE, Germany), freshly diluted exhaust (AIDE, Germany) and from aged aerosol downstream of the PEAR (Vaisala Carbocap GMP343, Finland) to determine and adjust the dilution ratios. Particulate emissions downstream of the PEAR were measured by HR-AMS and SMPS.

In the second experiments, aging of wood combustion emissions was studied using a PEAR flow rate of 60 L min^{-1} . Wood combustion emissions were generated by burning three consecutive batches (á 2.5 kg) of spruce logwood in a modern heat-storing masonry heater (Hiisi 4, Tulikivi Ltd., Finland), which was equipped with two-stage combustion air supply (Nuutinen et al. 2014). The wood combustion exhaust was diluted with a mean dilution ratio of 137, leading to mean primary PM, NO_x , and non-methane hydrocarbons (NMHC) concentrations of $518 \mu\text{g m}^{-3}$, 190, and 147 ppb, respectively. These levels are about 2–3 times higher than previously used in chamber experiments (Tiitta et al. 2016), but peak concentrations, especially during ignition, can increase the difference to chamber experiments to a temporary factor of 15. However, according to the study of Peng and Jimenez (2017) this should be still within atmospherically

relevant operating conditions for OFR apart from approximately 20 s after addition of new batch of logwood with OH reactivity (OHR) above 400 s^{-1} and NO concentrations of 150 ppb (see Section 3.6.). In addition, three batches (á 2 kg) of beech logwood were burned in a typical modern nonheat retaining chimney stove (Aduro 1.1, Denmark), which was also equipped with combustion air staging (Nussbaumer 2003). The ignition of the first batch was always conducted top-down using 150 g of spruce sticks as kindling. Dilution, sampling, and aging of the emissions were done in the same way as was done for the modern masonry heater experiments. The aged emissions were analyzed by HR-PTR-ToF-MS, HR-AMS, SMPS and CO_2 analyzers downstream of the PEAR.

3. Results and discussion

3.1. Flow conditions and RTDs

The velocity field and the residence time inside the PEAR were numerically simulated and the results were compared with the residence times obtained experimentally (Figure 3). Simulations and experiments were carried out for two total volume flows, 50 and 100 L min^{-1} . The simulated velocity fields show that with both flow rates there are only minor recirculation zones at the diffuser. The Reynolds number in the reactor section depends on the total flow, but is in laminar regime as Reynolds numbers account for 200 and 400 at 50 and 100 L min^{-1} flows, respectively. At the diffuser inlet, the Reynolds number of the flow is 7,000 and 14,000 for 50 and 100 L min^{-1} flows, respectively, indicating turbulent flow at the beginning of the diffuser. However, the aerosol residence time at

the narrow inlet with high Reynolds number is short (~ 10 ms) and therefore the high turbulence does not enhance aerosol losses in any significant extent.

As expected for viscous flows with wall interactions, the simulated residence times define a right-skewed distribution with global maxima at 95 and 62 s for 50 and 100 L min^{-1} , respectively. The mean residence times and their deviations are (140 ± 60) s and (70 ± 20) s for 50 and 100 L min^{-1} , respectively. The RTD maxima determined experimentally occur earlier than predicted by simulations (135 and 67 s with 50 and 100 L min^{-1} flows, respectively). This indicates that the flow field is not as optimum as the numerical simulations predicted and the flow recirculation and eddies are fairly stronger than anticipated, especially at the flow rate 50 L min^{-1} . Additionally, local maxima appear at the higher residence times in the RTD histogram. This undesirable feature may be caused by unpredictable diffuser performance at the 50 L min^{-1} , i.e. the backflow regions are substantially larger than predicted. Another probable cause of discrepancy between the measured and the simulated residence times is that the temperature differences are not included in the simulations and therefore natural convections arising from temperature gradient are excluded.

For comparison, a velocity field of a diffuser with too fast expansion rate is illustrated in Figure 3c. The results indicate severe flow separations from the wall causing substantial recirculation areas. In general, a shorter diffuser would be beneficial to have a more compact construction of the flow tube, but the simulations clearly show that with a short diffuser flow performance is not on the desired level and distinctly worse than in PEAR.

3.2. Particle losses

Stainless steel as conductive metal was chosen as wall material to reduce losses by electrostatic precipitation. The transmission efficiency of silver particles of different mobility diameters at flow rate of 50 and 100 L min^{-1} , are illustrated in Figure 4. Particles with mobility diameters larger than 50 nm are transmitted with 90–100% efficiency, which is considerably higher than reported for example by Lambe et al. (2011) for the PAM tube constructed of nonconductive Pyrex tube. The transmission efficiency noticeably declines for smaller particles whose predominant loss mechanism is diffusion. However, transmission efficiencies above 50% were measured even for 20 nm particles at a flow of 50 L min^{-1} and above 70% at 100 L min^{-1} .

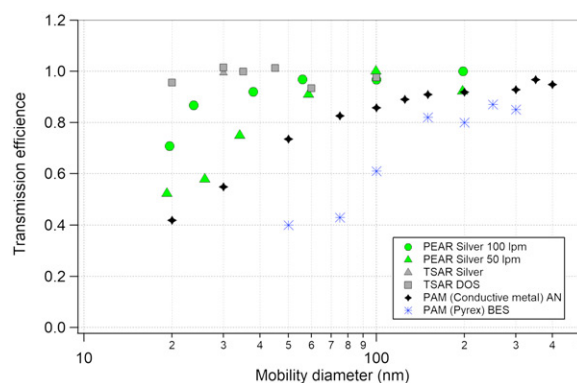


Figure 4. Size dependency of transmission efficiency for silver particles at flow rates of 100 L min^{-1} (circles) and 50 L min^{-1} (triangles) in PEAR (green) and literature data of transmission efficiencies for OFR Potential Aerosol Mass reactors (PAM) with Pyrex (blue; Lambe et al. 2011) and conductive metal chambers (black; Karjalainen et al. 2016), as well as for TUT Secondary Aerosol Reactor (TSAR) (grey; Simonen et al. 2017). The literature data consists of measurements using silver particles, dioctyl sebacate (DOS), Ammonium nitrate (AN) and bis(2-ethylhexyl) sebacate (BES) as test aerosols.

The lower losses at 100 L min^{-1} can be explained by more optimized flow conditions as indicated in Figure 3. Although those small particles account only for a low amount of total particle mass, they are highly relevant for aerosol emission toxicology in exposure studies, as they penetrate the respiratory system deeply from the extrathoracic region through to alveoli (Heyder 2004).

3.3. Relations between OH exposure, relative humidity, UV lamp voltage, and ozone concentration

The OH exposures in the flow tube with varying operating parameters are shown in Figure 5(left). During variation of the ozone concentration and the UV lamp output power, the relative humidity was maintained at $50 \pm 2\%$. The OH exposure increases proportional to increasing UV lamp driving voltage with higher slopes at higher ozone feed concentrations. As an upper limit, OH exposure corresponding to photochemical aging up to 14 days can be achieved at 50% relative humidity. In the following, an average OH concentration of 1×10^6 molec cm^{-3} (Prinn et al. 2001) for typical boundary layer conditions was used when photochemical ages are presented. Furthermore, the relative humidity also affected the OH exposure, but less than UV lamp power or ozone concentration. A linear relation between photochemical age and relative humidity was observed (Figure 5, right), similar to previous studies (Kang, Root, and Brune 2007).

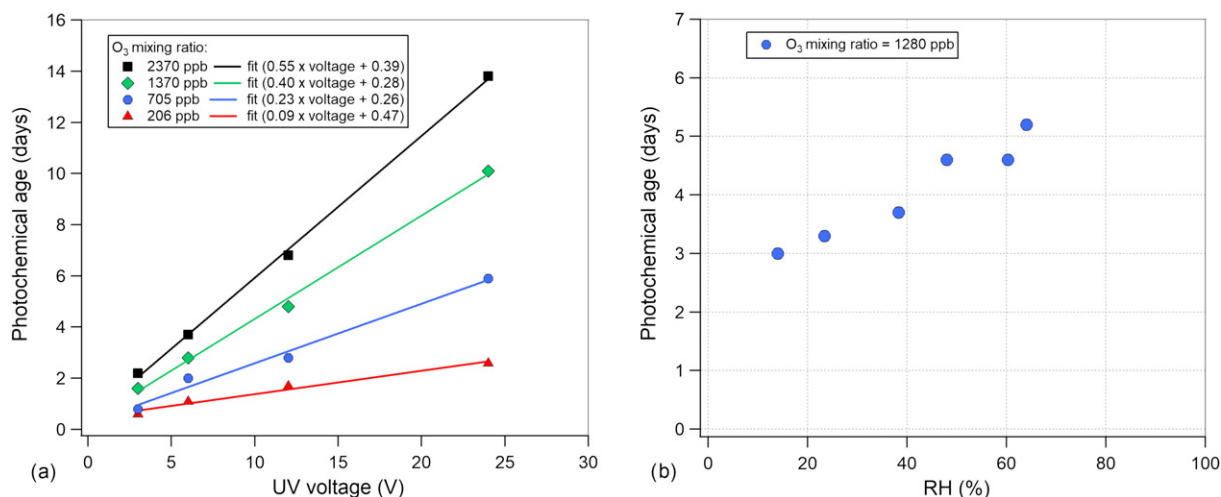


Figure 5. UV lamp voltage vs. photochemical age at (a) different ozone levels and 50% relative humidity, and (b) relation of photochemical age vs relative humidity (RH) at fixed UV lamp voltage of 4×3 V and ozone feed concentration of 1280 ppb. Both results were obtained from SO₂ degradation and using flow rate of 100 lpm. To calculate photochemical age, ambient OH concentration of 10^6 molec cm⁻³ was used.

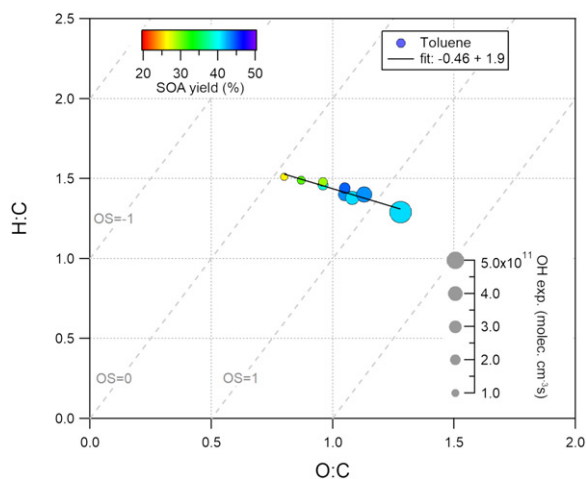


Figure 6. Van-Krevelen diagram of OA obtained from toluene photochemical aging. SOA yield and OH exposure are represented by color code and marker size, respectively.

3.4. Toluene photochemical aging

Toluene is an important anthropogenic SOA precursor in the atmosphere (Bruns et al. 2016) and is emitted in considerable amounts from a variety of sources, such as traffic and biomass combustion (Andreae and Merlet 2001; Saliba et al. 2017). Steady-state experiments were conducted with initial toluene concentrations of 94 and 230 ppb, and OH exposures in the range $0.8\text{--}3.5 \times 10^{11}$ molec cm⁻³ s (Figure 6). SOA yields for high-toluene experiments started to decrease from maximum value of 43% when OH exposure exceeded 3.2×10^{11} molec cm⁻³ s. This phenomenon has been also observed qualitatively in other previous aging experiments with toluene (Simonen et al. 2017) and α -pinene, which was addressed to an enhanced

importance of fragmentation relative to decreased vapor pressures by functionalization (Lambe et al. 2015). For low-toluene experiments, a linear relation between OH exposure and SOA yield was obtained, while for high-toluene decreasing yields were obtained for OH exposure $> 3 \times 10^{11}$ molec cm⁻³ s. The absolute SOA yield of aging toluene without seed aerosol and NO_x agrees well with an experiment done at ILMARI smog chamber (Leskinen et al. 2015), but appears to be higher than observed for aging studies with other OFR (Simonen et al. 2017). A possible explanation for the relatively high SOA yields is the low losses of LVOC and ultrafine particles in the PEAR system. Apparently, OS_C of toluene SOA appears slightly lower in other flow reactors at similar OH exposure (Simonen et al. 2017) (online Supplemental Information, Figure S2). In other words, high OS_C can be achieved in PEAR at lower OH exposure. However, it should be noted that, compared to the PEAR, the flow tubes discussed by Simonen et al. (2017) differ in several important design and experimental parameters. Therefore, we cannot unambiguously elucidate the bias in the relation between OH exposure and OS_C.

3.5. Aging of emissions from a spark-ignition engine

The oxidation of the DISI engine emissions were conducted with the engine cycle (NEDC) and steady states resembling the car driving at 80 or 120 km h⁻¹ with configured exposures from 0 to 7.3×10^{11} molec cm⁻³ s, equivalent to 0–8.4 days of atmospheric

photochemical aging. Moreover, emissions from EC were exposed to only ozone, and the emissions of constant 120 km h⁻¹ to only UV light. The results are summarized in Figure 7, depicting the dependence between photochemical age and OS_C as well as the enhancement in mass after aging. POA from EC featured slightly higher OS_C of -1.0 compared to steady state emissions at 80 and 120 km h⁻¹, with OS_C of -1.3 and -1.4, respectively. After aging, the OS_C for all emissions were substantially enhanced with an approximate increase in OS_C per day of photochemical aging of 0.2 d⁻¹ for EC and 0.5 d⁻¹ for 80 km h⁻¹. Simultaneously, initial OA concentrations of 102 μg m⁻³ (EC), 98 μg m⁻³ (120 km h⁻¹) and 67 μg m⁻³ (80 km h⁻¹) increased with enhancement ratios (ER_{OA}, defined as ratio of aged OA to nonaged OA), between 2.6 and 2.8 in all experiments with photochemical aging equivalent to 3–4 days. Higher OH exposure up to 8.4 days had only a small additional effect, and led to overall ER_{OA} of 3.1. All these ER_{OA} are distinctly lower than those reported at similar OH exposures in previous studies (Karjalainen et al. 2016; Pieber et al. 2018b; Timonen et al. 2017), which can be likely addressed to the hot start condition for the engine, the fact that no real car on a dynamometer was investigated, and in case of Pieber et al. (2018b) a different fuel with less than 0.5% of ethanol was used. Compared to continuous driving, the cold start included in NEDC produces orders of magnitude higher VOC emissions (Drozd et al. 2016), many of which are potential SOA precursors (Jathar et al. 2013).

The representativeness of OFR for tropospheric chemistry when studying engine emissions was evaluated in a recent study (Peng and Jimenez 2017). It was concluded that the usage of too low dilution may lead to too high concentrations of NO_x, which can dominate the subsequent reactions of peroxy radicals (RO₂) (Peng and Jimenez 2017). However, because of limited data in these experiments we can only refer to previous experiments with the same fuel (E10). In particular during the starting phase of the engine, high concentrations of VOCs together with NO_x are released due to a three-way catalyst below optimal working temperature (Karjalainen et al. 2016). Therefore, reactions which do not occur in the troposphere account for a substantial fraction of the possible reaction pathways (Peng and Jimenez 2017), but turn into more realistic chemistry ranges at hot conditions which were used in this study. Due to VOC concentrations below the limits of quantification of the gas analyzers used, we estimated the OHR assuming a

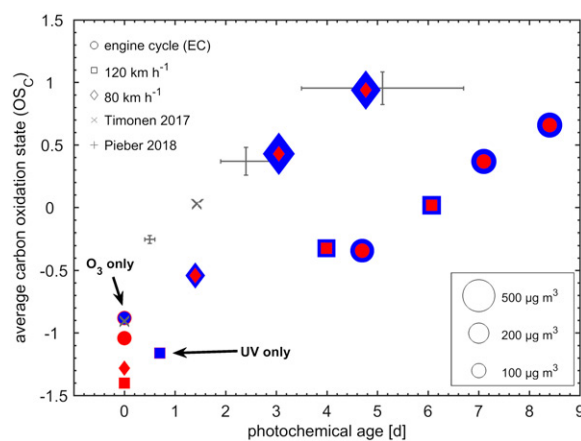


Figure 7. Photochemical age vs. average carbon oxidation state (OS_C) of emissions from DISI engine operated in engine cycle (EC, circles) or constant power related to 120 km h⁻¹ (squares) or 80 km h⁻¹ (diamonds). The size of the symbols represents the concentration of emitted POA (red) and OA mass after aging (blue). Blue core and red coating denote experiments with lower mass after aging than POA. For comparison, data from Pieber et al. (2018b) (GDI car, NEDC, SN EN 228 fuel) and Timonen et al. (2017) (GDI car, NEDC, E10 fuel) is added.

fixed ratio of VOC to CO. With the measured CO concentrations, OHR of 76 s⁻¹ were derived based on the data of Karjalainen et al. (2016). At a dilution factor of 40, NO_x concentration was below 100 ppb inside the PEAR, OHR of less than 100 s⁻¹, and a photon flux at 254 nm at maximum 1.8 10¹⁶ photons cm⁻² s⁻¹. Based on these values, we get an estimate “MHHH conditions” (medium [M] water mixing ratio, high [H] photon flux, high [H] OHR, high [H] NO) for our experiments, which appear in the “good” low-NO range, thus covering tropospheric relevant oxidation conditions (Peng and Jimenez 2017).

Short experiments in which either UV light or ozone was removed were carried out to check the effects of “UV only” and “O₃ only” on the results. In both of the conditions only slight changes in the sample aerosol were observed: both cases led only to slight increases in OS_C and even decrease in OA mass. A substantial fraction of components in DISI engine exhaust belongs to alkanes, parent and alkylated aromatics, which do not or react very slowly with ozone (Atkinson and Arey 2003). Volatile alkenes in gasoline emissions exposed to ozone form several volatile oxygenated species, but their contribution to the total SOA formation is likely small (Yang et al. 2018). Under condition “UV only,” almost no change in OA mass was obtained, but photochemical age reached 0.7 days. D9-butanol absorbs light weakly at 254 nm, so its degradation cannot be explained by photolysis. More likely, DISI engine emission constituents from

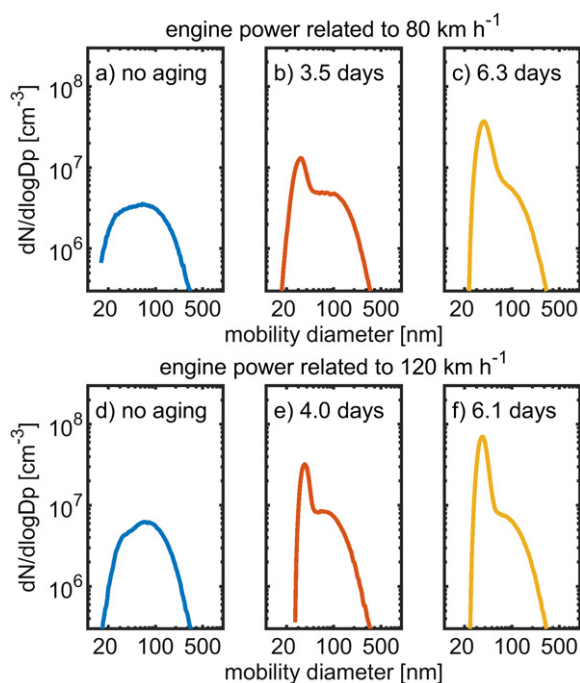


Figure 8. Particle size distributions for constant engine power resembling to 80 km h^{-1} (a–c) and 120 km h^{-1} (d–f) at different photochemical ages measured by SMPS. Measurements of aged and nonaged emissions are not done simultaneously.

E10 combustion, such as form- and acetaldehyde (Graham, Belisle, and Baas 2008), are photolyzed by the spectrum of the UV lamps between 250 and 450 nm (Figure S1, online Supplemental Information). The formed radicals may directly contribute to the degradation of d9-butanol, or form OH via the OH_x cycle (Ehhalt 1999).

Primary particle emissions revealed size modes in the ultrafine region of 64 and 69 nm for constant engine power resembling 80 and 120 km h^{-1} , respectively, with higher number concentrations at 120 km h^{-1} , which agrees well with observations from real gasoline cars on a dynamometer running on E10 fuel (Karjalainen et al. 2016; Timonen et al. 2017). After photochemical aging, new distinct modes of 36 and 39 nm, formed via nucleation, arose from the broader size distribution of the primary emissions (Figure 8). These small nucleation mode particles have been also observed in smog chamber studies for shortly aged gasoline emissions, but to disappear by coagulation and/or condensation of vapors after longer chamber residence times, while in aging flow reactors with orders of magnitudes lower residence times and faster gas-to-particle conversion, the nucleation mode particles are clearly visible (Bruns et al. 2015; Simonen et al. 2017). This feature of OFR is not representing real aerosol dynamics and size distributions of aged emission aerosols in the atmosphere, but can be useful

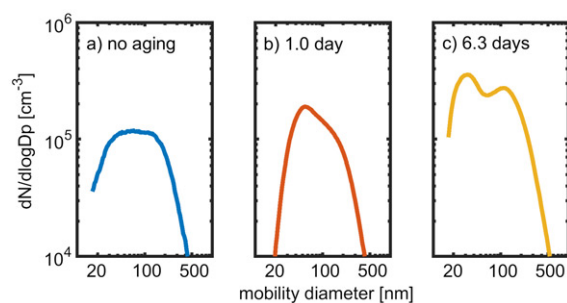


Figure 9. Particle size distributions of spruce logwood combustion emissions at different photochemical ages measured by SMPS.

in characterization of source-specific aerosols. However, when more realistic aerosol size distributions of highly aged aerosols are needed (e.g. toxicological exposure studies), the usage of additional seed aerosols may be used to provide additional surface area, to enhance condensation of vapors on existing particles and thereby to prevent nucleation of vapors.

3.6. Wood combustion SOA and comparison of SOA from PEAR and ILMARI smog chamber

Combustion aerosol from three consecutive batches of spruce logwood was aged in the PEAR using OH exposures from 0.8 to $6 \cdot 10^{11} \text{ molec cm}^{-3} \text{ s}$, equivalent to 0.9–7 days of atmospheric aging. Photochemical aging in PEAR led to ER_{OA} of 2.1–2.7, with highest values at lower OH exposures of 0.8 – $1.8 \cdot 10^{11} \text{ molec cm}^{-3} \text{ s}$. These findings agree well with ER_{OA} of 1.8–2.1 seen from the same modern masonry heater and spruce logwood at OH exposures of 0.5 – $0.7 \cdot 10^{11} \text{ molec cm}^{-3} \text{ s}$ in ILMARI smog chamber (Tiitta et al. 2016), indicating slightly higher SOA formation and/or lower loss in PEAR. The decline of ER_{OA} towards higher OH exposure may be explained by chemistry shifting from functionalization and subsequent condensation to heterogeneous oxidation with fragmentation and evaporation of secondary species of higher volatility (Ortega et al. 2016).

Particle number concentrations increased towards higher OH exposures via formation of particles in the size range of 10–50 nm at photochemical age of 6.3 days, leading to a bimodal size distribution (Figure 9). However, this nucleation mode particle formation was less pronounced than observed from aging of engine emissions.

Regarding SOA EF related to the mass of burned logwood, 30% lower SOA-EF were obtained for PEAR-aged OA (59 – 61 mg kg^{-1}) than for smog chamber-aged OA with similar wood fuel and combustion procedure (91 mg kg^{-1}) (Tiitta et al. 2016). SOA

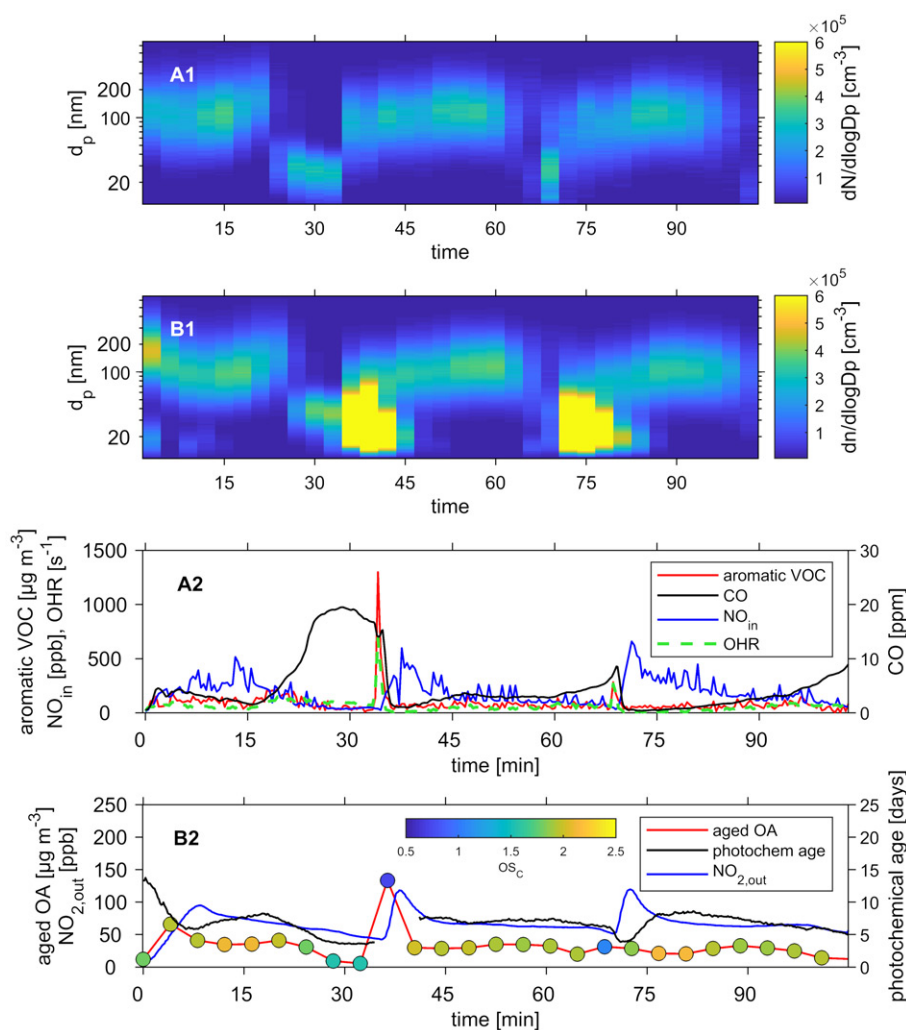


Figure 10. Particle number size distribution of primary (A1) and aged emissions (B1; 6.3 d of photochemical aging), derived from SMPS. Primary emissions of aromatic VOC (summed concentrations of SOA precursors benzene, toluene, xylenes and mesitylenes derived from FTIR), CO, NO and OH reactivity (OHR) are illustrated in A2. OA with OS_C , NO_2 and the photochemical age (derived from the decay of d9-butanol) of photochemically processed emissions are illustrated in B2. All concentrations are related to exhaust sample either entering or leaving PEAR with an average dilution ratio of 137.

formation depends strongly on the concentration and SOA formation potential of the released precursors (Bruns et al. 2016). Batchwise wood combustion is sensitive to the progress of burning shortly after the ignition (Czech et al. 2016), leading to considerable variation of the precursor VOCs. Therefore, the comparison between PEAR and smog chamber experiments should be rather based on ER_{OA} than SOA-EF. One of the advantages of using OFR with well-developed laminar flow profile and relatively short residence time is that it enables to study the influence of aging and SOA formation potential of sources with changing emission concentrations, such as cars emissions on driving cycles, wood combustion or ambient air in road tunnel (Karjalainen et al. 2016; Keller and Burtscher 2012; Tkacik et al. 2014). Figure 10 depicts the temporal profiles of spruce logwood combustion

emissions, including primary and secondary particle number distributions, aromatic VOC concentrations (measured directly from the flue gas stack), aged OA concentrations, and OA oxidation states at a photochemical age of 6.3 days. At the beginning, the concentrations of aromatic VOC are relatively low and stable, as a result of proper ignition of the logwood. From the ignition until the flaming phase primary particles with a mode of approximately 120 nm are released from the stove, which decrease in size when the flaming phase turn into glowing embers. The addition of subsequent logwood batches causes clearly visible peaks of aromatic VOC concentrations up to $1350 \mu\text{g m}^{-3}$. The high abundance of aromatic VOC, which are regarded as potent SOA precursor (Bruns et al. 2016), explains the observed new particle formation in the size of 10–60 nm. However, sharply

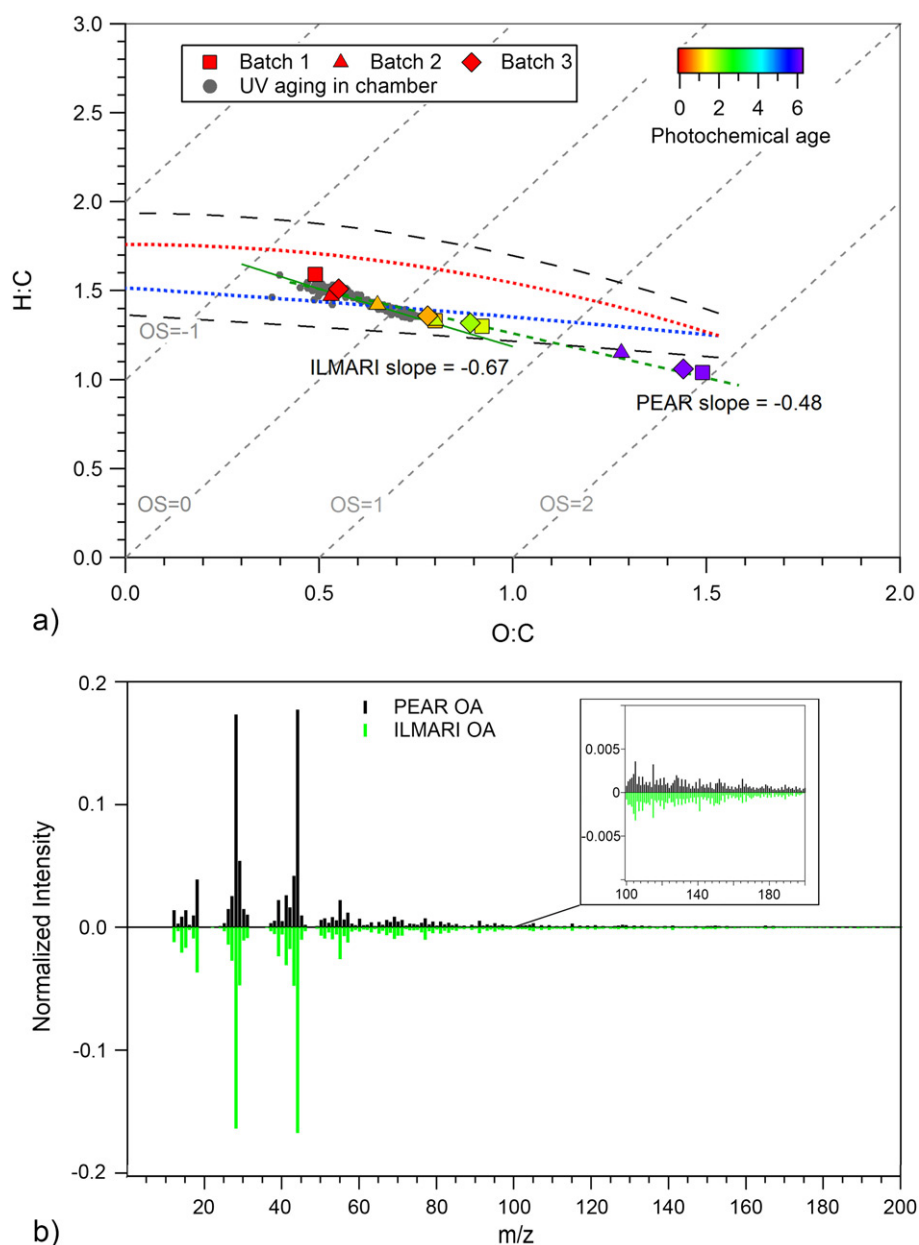


Figure 11. Van-Krevelen diagram on emission from batchwise combustion of spruce aged in PEAR and first batch aged in ILMARI smog chamber with a final photochemical age of 0.9 and 0.8 days (for fast and slow ignition, respectively, corresponding to experiments “4B” and “5B” of Tiitta et al. 2016). Aerosol mass spectra (PEAR: black; ILMARI smog chamber: green) reveal high similarity with a dot product of 0.99. The dotted lines define the triangular space where ambient OA components are typically located, including $\pm 10\%$ uncertainty in the parameterization (black dotted lines) (Ng et al. 2010, 2011).

increasing OA downstream of the PEAR features a distinct lower OS_C of +1 compared to aged OA during flaming conditions. This can be explained by two factors. First, the high VOC emissions exhibit a high OH radical consumption, leading to temporarily lower OH exposure when compared to other combustion phases. Second, the ignition of a new batch of logwood generates high POA emissions with O:C of roughly 0.5 (Heringa et al. 2012), which may oxidize heterogeneously (Tiitta et al., 2016) but likely slower than gas-phase species. Thus, the observed aged OA

downstream of the PEAR is hypothetically a mixture of less oxidized aged POA and more oxidized SOA. As a whole, the data shows that PEAR with a relatively narrow RTD is also capable to follow the dynamic changes of logwood combustion emissions and thus, can be used to investigate the role of different batchwise-fired logwood stove burning phases (Czech et al. 2016) on secondary aerosol formation.

The aging experiment was further investigated for relevancy of the reactions for tropospheric conditions. On that account, the OHR, here defined as the

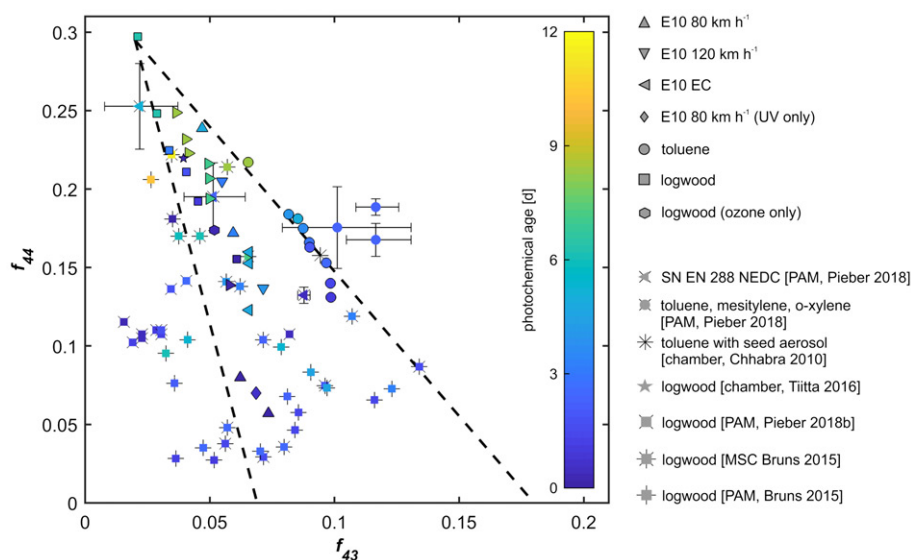


Figure 12. Triangular space in which OA of Northern hemisphere usually appears (Ng et al. 2010) with data of aged OA from different sources. All experimental data appears within the triangular space, giving evidence for sound simulation of atmospheric aging by PEAR. Literature data was taken from Tiitta et al. (2016); Pieber et al. (2018a); Chhabra et al. (2015) and Bruns et al. (2015). Please note that the data of Bruns et al. refers to $f(\text{CO}_2^+)$ and $f(\text{C}_2\text{H}_3\text{O}^+)$ instead of f_{44} and f_{43} , respectively. For Chhabra et al. the photochemical age is unknown.

summed products of VOCs and CO concentrations and their respective kinetic constants, was calculated and used together with NO concentrations to assess the dominating chemistry of VOCs. In the previous studies by Peng and Jimenez (2017) and Peng et al. (2018), the authors have used a classification “good”, “risky,” and “bad” for OFR conditions based on the ratios of VOC photolysis (at 254 nm) and non-OH reactants to the reactions of VOC with OH radicals. In “good” conditions the nontropospheric reactions are unimportant for almost all VOC precursors, “risky” conditions can be problematic for some VOCs and “bad” conditions for most of VOCs. During long aging experiment with maximum UV intensity, conditions in PEAR can be classified as “risky” when photon flux to OH ratio was $4.3 \times 10^6 \text{ cm s}^{-1}$, indicating that nontropospheric reactions may occur for some VOCs. However, for toluene, which is one of the most important logwood combustion precursors, the fate by photolysis in relation to OH-driven reaction was assessed to be minor (<15% of toluene was assessed to be photolyzed), excluding the peak OHR periods. In addition, for benzene, which is another major combustion VOC, the fate by non-OH reactant in relation to OH-driven reaction was assessed to be similar to ambient conditions (Oxidation Flow Reactor Exposure Estimator 3.1 by Peng and Jimenez). Furthermore, reactions between NO and RO_2 are reduced by rapid oxidation of NO to NO_2 by ozone concentrations above 2000 ppb, which shortens

NO lifetime to $\approx 1 \text{ s}$ and consequently reduces the impact of NO on the oxidation chemistry. NO concentrations out the PEAR were always below the detection limit, so NO_x can be completely assigned to NO_2 . However, the detected concentration of NO_2 explains only about 25% of the NO, which entered the PEAR, while rest of NO_x was further oxidized and at least partially converted to particulate nitrate, mainly in the form of ammonium nitrate (online Supplemental Information, Figure S3).

The evolution of the OA during aging can be visualized in the Van-Krevelen diagram, in which the slopes of the (linear) functional relation between O:C and H:C can be used to distinguish between different reaction pathways (Heald et al. 2010). POA with an average oxidation state of -0.5 follows an almost straight line in the Van-Krevelen diagram (Figure 11, top) with a slope of -0.50 ± 0.03 upon aging, corresponding to formation of acid groups, either via C–C bond cleavage and addition of carboxylic group or without C–C bond cleavage (Ng et al. 2011). Moreover, maximum O:C can be achieved with average oxidation states of $+2$, which have been observed also in ambient aerosol (Ng et al. 2010).

The comparison of smog chamber-aged logwood combustion emissions with 0.8 days of photochemical aging (Tiitta et al. 2016) to the PEAR-aged wood combustion emissions with 0.9 days of photochemical age shows a similar average OS_C for both aerosols. The OA from both cases appear in the same Van-

Krevelen region (Figure 11, top). However, OA aged in the smog chamber had lower intermediate slopes, between -0.64 and -0.67 . This indicates that fragmentation reactions due to photolysis are slightly less pronounced in the smog chamber than in the PEAR, which is probably caused by different UV emission spectra and intensities of the UV lamps inside the PEAR and the ILMARI smog chamber (Leskinen et al. 2015). Nevertheless, AMS OA spectra of these differently aged wood combustion aerosols revealed a remarkably high similarity (Figure 11, bottom), which is also supported by a dot product between these spectra, normalized to unit vector length of >0.99 . For comparison, a dot product of 0.93 was obtained for nonaged OA and OA of 7 days of photochemical age. Thus, PEAR was found to produce similar aged organic aerosol as the smog chamber with the same wood combustion exhaust, which agrees with the comparison of PAM-tube and smog chamber presented by Bruns et al. (2015).

3.7. Evolution of aerosols from different sources over increasing photochemical ages

Toluene/DISI engine emissions and spruce/beech logwood combustion represent the ambient OA types hydrocarbon-like organic aerosol (HOA) and biomass burning aerosol (BBOA), respectively. In this section, they were combined to demonstrate consistency of experiments involving the same emission source and similar aging conditions, as well as to investigate the atmospheric fate of the emissions. The plot of intensities of m/z 43 (f_{43}) vs. m/z 44 (f_{44}) (relative to the total intensity) (Figure 12) reveals that all experiments under widespread aging conditions appear between the boundaries in which ambient aerosol of the Northern hemisphere is observed (Ng et al. 2010). This gives indications for sound simulation of atmospheric aging by the PEAR. The applied unit mass resolution for this analysis may slightly shift the location of the data points of the abscissa in negative direction, but negligibly the ordinate (Corbin et al. 2015). The mass spectrometric fragments m/z 43 and m/z 44 are associated with the ions $C_2H_3O^+/C_3H_7^+$ and CO_2^+ , respectively, which are linked to the extent of oxidation received by an aerosol. The fragments $C_2H_3O^+$ and CO_2^+ result from nonacid oxygenates and carboxylic acids/acyl peroxides, respectively, and $C_3H_7^+$ refers to fragments of hydrocarbons (Ng et al. 2010). Therefore, POA such as BBOA and HOA move to the upper left corner in the triangular plot, which is also observed for the experiments presented. At

higher photochemical ages, the oxidized organic aerosol (OOA), linked to SOA, approaches the vertex of the triangle after 7–8 days of photochemical aging. Interestingly, aged gasoline emissions do not appear as close as aged BBOA to the triangle vertex. This agrees with the observed higher average oxidation states of aged logwood emissions when compared to oxidation states of the aged gasoline emissions, as presented in the previous sections. Altogether, these results indicate also that the PEAR can generate SOA of similar chemical composition towards higher OH exposure as observed in atmospheric studies (Jimenez et al. 2009). However, in future there is a need to study with more details (at molecular level) both the particulate and gaseous aging products, to evaluate how representative the PEAR, and other OFR using high OH concentrations, are in simulating tropospheric aging of emissions. This is particularly important in studying combustion emissions with high concentrations of NO_x and VOC and when using low dilution, since at these conditions nontropospheric alkyl peroxide chemistry may occur, as shown by Peng and Jimenez (2017).

4. Conclusions

A novel high-volume OFR, called “PEAR,” was designed, constructed, and then characterized by means of CFD modeling. Its performance was evaluated in experiments with commonly used precursors of secondary particles and with dynamic real-world combustion emissions. Results from these experiments were compared to results from previous studies on aerosols aged in OFRs, smog chambers, and ambient air. The PEAR system can be operated with aerosol flow rates in the range $50\text{--}200\text{ L min}^{-1}$ and can photochemically process relatively high aerosol concentrations. These capabilities enable *in-vivo* and *in-vitro* exposure studies coupled with physicochemical aerosol measurements and offline sample collections. The PEAR enables improved simulation of aerosol exposure situations with aged emissions and is therefore a valuable facility for studies aimed at understanding the impact of emission atmospheric aging on human health. Additionally, it enables measurements on the temporal evolution of the photochemical aging of dynamic emissions, such as emissions produced from batch-wise fired wood combustion, due to the short sample residence times (around 1 min), and narrow sample RTD. The used high flow rates combined with laminar flow profile and low surface-to-volume ratio collectively reduce the loss of smaller particles ($<50\text{ nm}$) by diffusion. This is

an advantage of the system, since combustion-derived nanoparticles have been especially linked to effective lung deposition and adverse health effects. Despite having a greater volume than many other flow tubes with comparable mean aerosol residence times, the PEAR system is still portable and can be used to study the aging of emissions from immobile emission sources. Nevertheless, development of a more compact model of the presented PEAR is in the planning stage. Furthermore, being able to operate as a stand-alone unit in the field, it can be also used to investigate the aging of ambient air.

In general, OFRs have been criticized by the scientific community when used to simulate atmospheric aging of aerosols. This is mainly due to following reasons: unnaturally high exposures of OH and O₃, photolysis by low wavelength photons and suppression of heterogeneous aging mechanisms. Despite of these limitations, the results from this study show similar SOA yields and aerosol chemical compositions for PEAR when compared to SOA yields and chemical compositions obtained from smog chamber experiments at similar OH exposure levels. This finding is consistent with some previous studies (Bruns et al. 2015; Lambe et al. 2015) which also show good agreement between OFRs and smog chambers. Overall, the results from this study indicate that OFR methods can be valuable for evaluating the role of atmospheric aging on the health and environmental impacts of combustion emissions.

Acknowledgments

The authors thank Ervin Nippolainen, Liqing Hao and Timo Oksanen from the University of Eastern Finland, Gert Jakobi from the Helmholtz Zentrum München and the staff from the Faculty of Mechanical Engineering and Marine Technology at the University of Rostock for their technical support. We thank Daniel J. Lane for proof-reading of the manuscript, Harri Kokkola for his valuable comments, and Simone Pieber, Emily Bruns and Pauli Simonen for providing data for method intercomparison.

Funding

The authors gratefully acknowledge funding from the Academy of Finland projects ASTRO and NABCEA (Grants 304459, 296645), Helmholtz Impulse and Network Fund of the Helmholtz Association (Germany) and German Research Foundation (grant ZI 764/14-1).

References

Adeosun, J. T., and A. Lawal. 2009. Numerical and experimental studies of mixing characteristics in a T-junction

- microchannel using residence-time distribution. *Chem. Eng. Sci.* 64 (10): 2422–2432. doi:10.1016/j.ces.2009.02.013.
- Ahlberg, E., J. Falk, A. Eriksson, T. Holst, W. H. Brune, A. Kristensson, P. Roldin, and B. Svenningsson. 2017. Secondary organic aerosol from VOC mixtures in an oxidation flow reactor. *Atmos. Environ.* 161:210–220. doi:10.1016/j.atmosenv.2017.05.005.
- Andreae, M. O., and P. Merlet. 2001. Emission of trace gases and aerosols from biomass burning. *Global Biogeochem. Cycles.* 15 (4):955–966. doi:10.1029/2000GB001382.
- Asa-Awuku, A., M. A. Miracolo, J. H. Kroll, A. L. Robinson, and N. M. Donahue. 2009. Mixing and phase partitioning of primary and secondary organic aerosols. *Geophys. Res. Lett.* 36 (15). doi:10.1029/2009GL039301.
- Atkinson, R., and J. Arey. 2003. Atmospheric degradation of volatile organic compounds. *Chem. Rev.* 103 (12): 4605–4638. doi:10.1021/cr0206420.
- Barmet, P., J. Dommen, P. F. DeCarlo, T. Tritscher, A. P. Praplan, S. M. Platt, A. S. H. Prévôt, N. M. Donahue, and U. Baltensperger. 2012. OH clock determination by proton transfer reaction mass spectrometry at an environmental chamber. *Atmos. Meas. Tech.* 5 (3):647–656. doi:10.5194/amt-5-647-2012.
- Boucher, O. 2015. *Atmospheric aerosols: Properties and climate impacts.* Netherlands: Springer.
- Brockmann, J. E. 2001. Sampling and transport of aerosols. In *Aerosol measurement: Principles, techniques and applications*, ed. P. A. Baron and K. Willeke, 2nd ed., 143–95. Engineering professional collection. New York: Wiley.
- Bruns, E. A., I. El Haddad, A. Keller, F. Klein, N. K. Kumar, S. M. Pieber, J. C. Corbin, J. G. Slowik, W. H. Brune, U. Baltensperger, et al. 2015. Inter-comparison of laboratory smog chamber and flow reactor systems on organic aerosol yield and composition. *Atmos. Meas. Tech.* 8 (6):2315–2332. doi:10.5194/amt-8-2315-2015.
- Bruns, E. A., I. E. Haddad, J. G. Slowik, D. Kilic, F. Klein, U. Baltensperger, and A. S. H. Prévôt. 2016. Identification of significant precursor gases of secondary organic aerosols from residential wood combustion. *Sci. Rep.* 6 :27881. doi:10.1038/srep27881.
- Canagaratna, M. R., J. L. Jimenez, J. H. Kroll, Q. Chen, S. H. Kessler, P. Massoli, L. Hildebrandt Ruiz, E. Fortner, L. R. Williams, et al. 2015. Elemental ratio measurements of organic compounds using aerosol mass spectrometry: Characterization, improved calibration, and implications. *Atmos. Chem. Phys.* 15 (1):253–272. doi:10.5194/acp-15-253-2015.
- Chhabra, P. S., A. T. Lambe, M. R. Canagaratna, H. Stark, J. T. Jayne, T. B. Onasch, P. Davidovits, J. R. Kimmel, and D. R. Worsnop. 2015. Application of high-resolution time-offlight chemical ionization mass spectrometry measurements to estimate volatility distributions of α -pinene and naphthalene oxidation products. *Atmos. Meas. Tech.* 8 (1):1–18. doi:10.5194/amt-8-1-2015.
- Chirico, R., P. F. DeCarlo, M. F. Heringa, T. Tritscher, R. Richter, A. S. H. Prévôt, J. Dommen, E. Weingartner, G. Wehrle, M. Gysel, et al. 2010. Impact of aftertreatment devices on primary emissions and secondary organic aerosol formation potential from in-use diesel vehicles: Results from smog chamber experiments. *Atmos. Chem. Phys.* 10 (23):11545–11563. doi:10.5194/acp-10-11545-2010.

- Chu, B., J. Liggio, Y. Liu, H. He, H. Takekawa, S.-M. Li, and J. Hao. 2017. Influence of metal-mediated aerosol-phase oxidation on secondary organic aerosol formation from the ozonolysis and OH-Oxidation of α -Pinene. *Sci. Rep.* 7 :40311. doi:10.1038/srep40311.
- Corbin, J. C., A. Keller, U. Lohmann, H. Burtscher, B. Sierau, and A. A. Mensah. 2015. Organic emissions from a wood stove and a pellet stove before and after simulated atmospheric aging. *Aerosol Sci. Technol.* 49 (11): 1037–1050. doi:10.1080/02786826.2015.1079586.
- Czech, H., O. Sippula, M. Kortelainen, J. Tissari, C. Radischat, J. Passig, T. Streibel, J. Jokiniemi, and R. Zimmermann. 2016. On-line analysis of organic emissions from residential wood combustion with single-photon ionisation time-of-flight mass spectrometry (SPI-TOFMS). *Fuel* 177 :334–342. doi:10.1016/j.fuel.2016.03.036.
- Davis, D. D., A. R. Ravishankara, and S. Fischer. 1979. SO₂ oxidation via the hydroxyl radical atmospheric fate of HSO_x radicals. *Geophys. Res. Lett.* 6 (2):113–116. doi:10.1029/GL006i002p00113.
- Delfino, R. J., N. Staimer, T. Tjoa, M. Arhami, A. Polidori, D. L. Gillen, S. C. George, M. M. Shafer, J. J. Schauer, and C. Sioutas. 2010. Associations of primary and secondary organic aerosols with airway and systemic inflammation in an elderly panel cohort. *Epidemiology.* 21 (6): 892–902. doi:10.1097/EDE.0b013e3181f20e6c.
- Drozd, G. T., Y. Zhao, G. Saliba, B. Frodin, C. Maddox, R. J. Weber, M.-C. O. Chang, H. Maldonado, S. Sardar, A. L. Robinson, et al. 2016. Time resolved measurements of speciated tailpipe emissions from motor vehicles: Trends with emission control technology, cold start effects, and speciation. *Environ. Sci. Technol.* 50 (24): 13592–13599. doi:10.1021/acs.est.6b04513.
- Ehhalt, D. H. 1999. Photooxidation of trace gases in the troposphere. *Phys. Chem. Chem. Phys.* 1 (24):5401–5408. doi:10.1039/a905097c.
- El-Beheri, S. M., and M. H. Hamed. 2009. A comparative study of turbulence models performance for turbulent flow in a planar asymmetric diffuser. *World. Acad. Sci. Eng. Technol.* 53 :769–780.
- Ezell, M. J., H. Chen, K. D. Arquero, and B. J. Finlayson-Pitts. 2014. Aerosol fast flow reactor for laboratory studies of new particle formation. *J. Aerosol Sci.* 78 :30–40. doi:10.1016/j.jaerosci.2014.08.009.
- Ezell, M. J., S. N. Johnson, Y. Yu, V. Perraud, E. A. Bruns, M. L. Alexander, A. Zelenyuk, D. Dabdub, and B. J. Finlayson-Pitts. 2010. A new aerosol flow system for photochemical and thermal studies of tropospheric aerosols. *Aerosol Sci. Technol.* 44 (5):329–338. doi:10.1080/02786821003639700.
- Fuchs, N. A., and A. G. Sutugin. 1971. Highly dispersed aerosols. In *Topics in current aerosol research*, ed. G. M. Hidy and J. R. Brock, 1–60. New York: Pergamon.
- George, I. J., A. Vlasenko, J. G. Slowik, K. Broekhuizen, and J. P. D. Abbatt. 2007. Heterogeneous oxidation of saturated organic aerosols by hydroxyl radicals: Uptake kinetics, condensed-phase products, and particle size change. *Atmos. Chem. Phys.* 7 (16):4187–4201. doi:10.5194/acp-7-4187-2007.
- Graham, L. A., S. L. Belisle, and C.-L. Baas. 2008. Emissions from light duty gasoline vehicles operating on low blend ethanol gasoline and E85. *Atmos. Environ.* 42 (19): 4498–4516. doi:10.1016/j.atmosenv.2008.01.061.
- Gullett, B. K., L. Oudejans, and A. Touati. 2013. Real-Time measurement of trace air toxic vehicular emissions by REMPI-TOFMS during dynamometer driving cycles. *Aerosol Air Qual. Res.* 13 (4):1170–1180. doi:10.4209/aaqr.2012.12.0345.
- Happo, M. S., O. Sippula, P. I. Jalava, H. Rintala, A. Leskinen, M. Komppula, K. Kuuspallo, S. Mikkonen, K. Lehtinen, J. Jokiniemi, et al. 2014. Role of microbial and chemical composition in toxicological properties of indoor and outdoor air particulate matter. *Part Fibre Toxicol.* 11 :60. doi:10.1186/s12989-014-0060-6.
- Heald, C. L., J. H. Kroll, J. L. Jimenez, K. S. Docherty, P. F. DeCarlo, A. C. Aiken, Q. Chen, S. T. Martin, D. K. Farmer, and P. Artaxo. 2010. A simplified description of the evolution of organic aerosol composition in the atmosphere. *Geophys. Res. Lett.* 37 (8):8350. doi:10.1029/2010GL042737.
- Heringa, M. F., P. F. DeCarlo, R. Chirico, A. Lauber, A. Doberer, J. Good, T. Nussbaumer, A. Keller, H. Burtscher, et al. 2012. Time-resolved characterization of primary emissions from residential wood combustion appliances. *Environ. Sci. Technol.* 46 (20):11418–11425. doi:10.1021/es301654w.
- Heyder, J. 2004. Deposition of inhaled particles in the human respiratory tract and consequences for regional targeting in respiratory drug delivery. *Proc. Am. Thorac. Soc.* 1 (4):315–320. doi:10.1513/pats.200409-046TA.
- Huang, R.-J., Y. Zhang, C. Bozzetti, K.-F. Ho, J.-J. Cao, Y. Han, K. R. Daellenbach, J. G. Slowik, S. M. Platt, F. Canonaco, et al. 2014. High secondary aerosol contribution to particulate pollution during haze events in China. *Nature.* 514 (7521):218–222. doi:10.1038/nature13774.
- Huang, W., J. Cao, Y. Tao, L. Dai, S.-E. Lu, B. Hou, Z. Wang, and T. Zhu. 2012. Seasonal variation of chemical species associated with short-term mortality effects of PM(2.5) in Xi'an, a Central city in China. *Am. J. Epidemiol.* 175 (6):556–566. doi:10.1093/aje/kwr342.
- Jathar, S. H., B. Friedman, A. A. Galang, M. F. Link, P. Brophy, J. Volckens, S. Eluri, and D. K. Farmer. 2017. Linking load, fuel, and emission controls to photochemical production of secondary organic aerosol from a diesel engine. *Environ. Sci. Technol.* 51 (3):1377–1386. doi:10.1021/acs.est.6b04602.
- Jathar, S. H., M. A. Miracolo, D. S. Tkacik, N. M. Donahue, P. J. Adams, and A. L. Robinson. 2013. Secondary organic aerosol formation from photo-oxidation of unburned fuel: Experimental results and implications for aerosol formation from combustion emissions. *Environ. Sci. Technol.* 47 (22):12886–12893. doi:10.1021/es403445q.
- Jia, L., and Y. Xu. 2013. Effects of relative humidity on ozone and secondary organic aerosol formation from the photooxidation of benzene and ethylbenzene. *Aerosol Sci. Technol.* 48 (1):1–12. doi:10.1080/02786826.2013.847269.
- Jimenez, J. L., M. R. Canagaratna, N. M. Donahue, A. S. H. Prévôt, Q. Zhang, J. H. Kroll, P. F. DeCarlo, J.D. Allan, H. Coe, N.L. Ng, et al. 2009. Evolution of organic aerosols in the atmosphere. *Science.* 326 (5959):1522–1525. doi:10.1126/science.1179518.
- Kanashova, T., O. Sippula, S. Oeder, T. Streibel, J. Passig, H. Czech, T. Kaoma, S. Sapcaru, C. Sean, M. Dilger, et al. 2018. Emissions from a modern log wood masonry heater and wood pellet boiler: Composition and

- biological impact on air-liquid interface exposed human lung cancer cells. *J. Mol. Clin. Med.* 1 :23–35.
- Kang, E., M. J. Root, and W. H. Brune. 2007. Introducing the concept of potential aerosol mass (PAM). *Atmos. Chem. Phys. Discuss.* 7 (4):9925–9972. doi:10.5194/acpd-7-9925-2007.
- Karjalainen, P., H. Timonen, E. Saukko, H. Kuuluvainen, S. Saarikoski, P. Aakko-Saksa, T. Murtonen, M. Bloss, M. Dal Maso, P. Simonen, et al. 2016. Time-resolved characterization of primary particle emissions and secondary particle formation from a modern gasoline passenger car. *Atmos. Chem. Phys.* 16 (13):8559–8570. doi:10.5194/acp-16-8559-2016.
- Keller, A., and H. Burtscher. 2012. A continuous photo-oxidation flow reactor for a defined measurement of the SOA formation potential of wood burning emissions. *J. Aerosol Sci.* 49 :9–20. doi:10.1016/j.jaerosci.2012.02.007.
- Keller, A., and H. Burtscher. 2017. Characterizing particulate emissions from wood burning appliances including secondary organic aerosol formation potential. *J. Aerosol Sci.* 114 :21–30. doi:10.1016/j.jaerosci.2017.08.014.
- Kroll, J. H., N. M. Donahue, J. L. Jimenez, S. H. Kessler, M. R. Canagaratna, K. R. Wilson, K. E. Altieri, L. R. Mazzoleni, A. S. Wozniak, H. Bluhm, et al. 2011. Carbon oxidation state as a metric for describing the chemistry of atmospheric organic aerosol. *Nature Chem.* 3 (2): 133–139. doi:10.1038/nchem.948.
- Kroll, J. H., C. Y. Lim, S. H. Kessler, and K. R. Wilson. 2015. Heterogeneous oxidation of atmospheric organic aerosol: Kinetics of changes to the amount and oxidation state of particle-phase organic carbon. *J. Phys. Chem. A.* 119 (44):10767–10783. doi:10.1021/acs.jpca.5b06946.
- Künzi, L., M. Krapf, N. Daher, J. Dommen, N. Jeannet, S. Schneider, S. Platt, et al. 2015. Toxicity of aged gasoline exhaust particles to normal and diseased airway epithelia. *Sci. Rep.* 5 :11801. doi:10.1038/srep11801.
- Laden, F., L. M. Neas, D. W. Dockery, and J. Schwartz. 2000. Association of fine particulate matter from different sources with daily mortality in six U.S. Cities. *Environ. Health Perspect.* 108 (10):941. doi:10.2307/3435052.
- Lambe, A. T., A. T. Ahern, L. R. Williams, J. G. Slowik, J. P. S. Wong, J. P. D. Abbatt, W. H. Brune, N. L. Ng, J. P. Wright, D. R. Croasdale, et al. 2011. Characterization of aerosol photooxidation flow reactors: Heterogeneous oxidation, secondary organic aerosol formation and cloud condensation nuclei activity measurements. *Atmos. Meas. Tech.* 4 (3):445–461. doi:10.5194/amt-4-445-2011.
- Lambe, A. T., P. S. Chhabra, T. B. Onasch, W. H. Brune, J. F. Hunter, J. H. Kroll, M. J. Cummings, J. F. Brogan, Y. Parmar, D. R. Worsnop, et al. 2015. Effect of oxidant concentration, exposure time, and seed particles on secondary organic aerosol chemical composition and yield. *Atmos. Chem. Phys.* 15 (6):3063–3075. doi:10.5194/acp-15-3063-2015.
- Lehtinen, K. E. J., H. Korhonen, M. Dal Maso, and M. Kulmala. 2003. On the concept of condensation sink diameter. *Boreal Environ. Res.* 8 :405–411.
- Leskinen, A., P. Yli-Pirilä, K. Kuusalo, O. Sippula, P. Jalava, M.-R. Hirvonen, J. Jokiniemi, A. Virtanen, M. Komppula, and K. E. J. Lehtinen. 2015. Characterization and testing of a new environmental chamber. *Atmos. Meas. Tech.* 8 (6): 2267–2278. doi:10.5194/amt-8-2267-2015.
- Li, R., B. B. Palm, A. M. Ortega, J. Hlywiak, Weiwei Hu, Z. Peng, D. A. Day et al. 2015. Modeling the radical chemistry in an oxidation flow reactor: radical formation and recycling, sensitivities, and the OH exposure estimation equation. *J. Phys. Chem. A* 119 (19):4418–4432. doi:10.1021/jp509534k.
- Lyyrinen, J., J. Jokiniemi, E. I. Kauppinen, U. Backman, and H. Vesala. 2004. Comparison of different dilution methods for measuring diesel particle emissions. *Aerosol Sci. Technol.* 38 (1):12–23. doi:10.1080/02786820490247579.
- Maier, K. L., F. Alessandrini, I. Beck-Speier, T. P. Josef Hofer, S. Diabaté, E. Bitterle, T. Stöger, T. Jakob, H. Behrendt, M. Horsch, et al. 2008. Health effects of ambient particulate matter—Biological mechanisms and inflammatory responses to in vitro and in vivo particle exposures. *Inhal. Toxicol.* 20 (3):319–337. doi:10.1080/08958370701866313.
- Myhre, G., T. F. Berglen, M. Johnsrud, C. R. Hoyle, T. K. Berntsen, S. A. Christopher, D. W. Fahey, I. S. A. Isaksen, T. A. Jones, R. A. Kahn, et al. 2009. Modelled radiative forcing of the direct aerosol effect with multi-observation evaluation. *Atmos. Chem. Phys.* 9 (4): 1365–1392. doi:10.5194/acp-9-1365-2009.
- Ng, N. L., M. R. Canagaratna, J. L. Jimenez, P. S. Chhabra, J. H. Seinfeld, and D. R. Worsnop. 2011. Changes in organic aerosol composition with aging inferred from aerosol mass spectra. *Atmos. Chem. Phys.* 11 (13): 6465–6474. doi:10.5194/acp-11-6465-2011.
- Ng, N. L., M. R. Canagaratna, Q. Zhang, J. L. Jimenez, J. Tian, I. M. Ulbrich, J. H. Kroll, K. S. Docherty, P. S. Chhabra, R. Bahreini, et al. 2010. Organic aerosol components observed in Northern hemispheric datasets from aerosol mass spectrometry. *Atmos. Chem. Phys.* 10 (10): 4625–4641. doi:10.5194/acp-10-4625-2010.
- Nussbaumer, T. 2003. Combustion and Co-combustion of biomass: Fundamentals, Technologies, and primary measures for emission reduction. *Energy Fuels.* 17 (6): 1510–1521. doi:10.1021/ef030031q.
- Nuutinen, K., J. Jokiniemi, O. Sippula, H. Lamberg, J. Sutinen, P. Horttanainen, and J. Tissari. 2014. Effect of air staging on fine particle, dust and gaseous emissions from masonry heaters. *Biomass Bioenergy.* 67 :167–178. doi:10.1016/j.biombioe.2014.04.033.
- Obi, S., K. Aoki, S. Masuda, and K. Japan. 1993. Experimental and computational study of turbulent separating flow in an asymmetric plane diffuser. In *Ninth symposium on "Turbulent Shear Flows"*, P305-1–P305-4.
- Odum, J. R., T. Hoffmann, F. Bowman, D. Collins, R. C. Flagan, and J. H. Seinfeld. 1996. Gas/Particle partitioning and secondary organic aerosol yields. *Environ. Sci. Technol.* 30 (8):2580–2585. doi:10.1021/es950943+.
- Oeder, S., T. Kanashova, O. Sippula, S. C. Sapcaru, T. Streibel, J. M. Arteaga-Salas, J. Passig, M. Dilger, H.-R. Paur, C. Schlager, S. Mülhopt, et al. 2015. Particulate matter from both heavy fuel oil and diesel fuel shipping emissions show strong biological effects on human lung cells at realistic and comparable in vitro exposure conditions. *Plos One.* 10 (6):e0126536. doi:10.1371/journal.pone.0126536.
- Ortega, A. M., D. A. Day, M. J. Cubison, W. H. Brune, D. Bon, J. A. de Gouw, and J. L. Jimenez. 2013. Secondary organic aerosol formation and primary organic aerosol oxidation from biomass-burning smoke in a flow reactor

- during FLAME-3. *Atmos. Chem. Phys.* 13 (22): 11551–11571. doi:10.5194/acp-13-11551-2013.
- Ortega, A. M., P. L. Hayes, Z. Peng, B. B. Palm, W. Hu, D. A. Day, R. Li, M. J. Cubison, W. H. Brune, M. Graus, et al. 2016. Real-time measurements of secondary organic aerosol formation and aging from ambient air in an oxidation flow reactor in the los angeles area. *Atmos. Chem. Phys.* 16 (11):7411–7433. doi:10.5194/acp-16-7411-2016.
- Palm, B. B., P. Campuzano-Jost, A. M. Ortega, D. A. Day, L. Kaser, W. Jud, T. Karl, A. Hansel, J. F. Hunter, E. S. Cross, et al. 2016. In situ secondary organic aerosol formation from ambient pine Forest air using an oxidation flow reactor. *Atmos. Chem. Phys.* 16 (5):2943–2970. doi: 10.5194/acp-16-2943-2016.
- Paur, H.-R., F. R. Cassee, J. Teeguarden, H. Fissan, S. Diabate, M. Aufderheide, W. G. Kreyling, O. Hänninen, G. Kasper, M. Riediker, et al. 2011. In-vitro cell exposure studies for the assessment of nanoparticle toxicity in the lung—A dialog between aerosol science and biology. *J. Aerosol Sci.* 42 (10): 668–692. doi:10.1016/j.jaerosci.2011.06.005.
- Peng, Z., D. A. Day, A. M. Ortega, B. B. Palm, W. Hu, H. Stark, R. Li, K. Tsigaridis, W. H. Brune, and J. L. Jimenez. 2016. Non-OH chemistry in oxidation flow reactors for the study of atmospheric chemistry systematically examined by modeling. *Atmos. Chem. Phys.* 16 (7): 4283–4305. doi:10.5194/acp-16-4283-2016.
- Peng, Z., and J. L. Jimenez. 2017. Modeling of the chemistry in oxidation flow reactors with high initial NO. *Atmos. Chem. Phys.* 17 (19):11991–12010. doi:10.5194/acp-17-11991-2017.
- Peng, Z., B. B. Palm, D. A. Day, R. K. Talukdar, W. Hu, A. T. Lambe, W. H. Brune, and J. L. Jimenez. 2018. Model evaluation of new techniques for maintaining High-NO conditions in oxidation flow reactors for the study of OH-Initiated atmospheric chemistry. *ACS Earth Space Chem.* 2 (2):72–86. doi:10.1021/acsearthspacechem.7b00070.
- Pieber, S. M., A. Kambolis, D. Ferri, D. Bhattu, E. A. Bruns, M. Elsener, O. Kröcher, A. S. H. Prévôt, and U. Baltensperger. 2018a. Mitigation of secondary organic aerosol formation of log wood burning emissions by catalytic removal of aromatic hydrocarbons. *Environ. Sci. Technol.* (just accepted). doi:10.1021/acs.est.8b04124.
- Pieber, S. M., N. K. Kumar, F. Klein, P. Comte, D. Bhattu, J. Dommen, E. A. Bruns, D. Kılıç, I. El Haddad, A. Keller, et al. 2018b. Gas-phase composition and secondary organic aerosol formation from standard and particle filter-retrofitted gasoline direct injection vehicles investigated in a batch and flow reactor. *Atmos. Chem. Phys.* 18 (13):9929–9954. doi:10.5194/acp-18-9929-2018.
- Pope, C. A., R. T. Burnett, G. D. Thurston, M. J. Thun, E. E. Calle, D. Krewski, and J. J. Godleski. 2004. Cardiovascular mortality and long-term exposure to particulate air pollution: Epidemiological evidence of general pathophysiological pathways of disease. *Circulation.* 109 (1):71–77. doi:10.1161/01.CIR.0000108927.80044.7F.
- Pöschl, U. 2005. Atmospheric aerosols: Composition, transformation, climate and health effects. *Angew. Chem. Int. Ed. Engl.* 44 (46):7520–7540. doi:10.1002/anie.200501122.
- Prinn, R. G., J. Huang, R. F. Weiss, D. M. Cunnold, P. J. Fraser, P. G. Simmonds, A. McCulloch., et al. 2001. Evidence for substantial variations of atmospheric hydroxyl radicals in the past two decades. *Science* 292 (5523):1876–1882. doi:10.1126/science.1059495.
- Ramanathan, V., R. D. Cess, E. F. Harrison, P. Minnis, B. R. Barkstrom, E. Ahmad, and D. Hartmann. 1989. Cloud-radiative forcing and climate: Results from the earth radiation budget experiment. *Science* 243 (4887): 57–63. doi:10.1126/science.243.4887.57.
- Saliba, G., R. Saleh, Y. Zhao, A. A. Presto, A. T. Lambe, B. Frodin, S. Sardar, H. Maldonado, C. Maddox, A. A. May, et al. 2017. Comparison of gasoline direct-injection (GDI) and port fuel injection (PFI) vehicle emissions: Emission certification standards, cold-start, secondary organic aerosol formation potential, and potential climate impacts. *Environ. Sci. Technol.* 51 (11):6542–6552. doi: 10.1021/acs.est.6b06509.
- Shiraiwa, M., K. Ueda, A. Pozzer, G. Lammel, C. J. Kampf, A. Fushimi, S. Enami, A. M. Arangio, J. Fröhlich-Nowoisky, Y. Fujitani, et al. 2017. Aerosol health effects from molecular to global scales. *Environ. Sci. Technol.* 51 (23):13545–13567. doi:10.1021/acs.est.7b04417.
- Simonen, P., E. Saukko, P. Karjalainen, H. Timonen, M. Bloss, P. Aakko-Saksa, T. Rönkkö, J. Keskinen, and M. Dal Maso. 2017. A new oxidation flow reactor for measuring secondary aerosol formation of rapidly changing emission sources. *Atmos. Meas. Tech.* 10 (4):1519–1537. doi:10.5194/amt-10-1519-2017.
- Sparrow, E. M., J. P. Abraham, and W. J. Minkowycz. 2009. Flow separation in a diverging conical duct: Effect of Reynolds number and divergence angle. *Int. J. Heat Mass Transf.* 52 (13–14):3079–3083. doi:10.1016/j.ijheatmasstransfer.2009.02.010.
- Tiitta, P., A. Leskinen, L. Hao, P. Yli-Pirilä, M. Kortelainen, J. Grigonyte, J. Tissari, H. Lamberg, A. Hartikainen, K. Kuuspalo, et al. 2016. Transformation of logwood combustion emissions in a smog chamber: Formation of secondary organic aerosol and changes in the primary organic aerosol upon daytime and nighttime aging. *Atmos. Chem. Phys.* 16 (20):13251–13269. doi:10.5194/acp-16-13251-2016.
- Timonen, H., P. Karjalainen, E. Saukko, S. Saarikoski, P. Aakko-Saksa, P. Simonen, T. Murtonen, M. Dal Maso, H. Kuuluvainen, M. Bloss, et al. 2017. Influence of fuel ethanol content on primary emissions and secondary aerosol formation potential for a modern flex-fuel gasoline vehicle. *Atmos. Chem. Phys.* 17 (8):5311–5329. doi: 10.5194/acp-17-5311-2017.
- Tkacik, D. S., A. T. Lambe, S. Jathar, X. Li, A. A. Presto, Y. Zhao, D. Blake, S. Meinardi, J. T. Jayne, P. L. Croteau, and A. L. Robinson. 2014. Secondary organic aerosol formation from in-Use motor vehicle emissions using a potential aerosol mass reactor. *Environ. Sci. Technol.* 48 (19):11235–11242. doi:10.1021/es502239v.
- Verma, V., Z. Ning, A. K. Cho, J. J. Schauer, M. M. Shafer, and C. Sioutas. 2009. Redox activity of urban quasi-ultrafine particles from primary and secondary sources. *Atmos. Environ.* 43 (40):6360–6368. doi:10.1016/j.atmosenv.2009.09.019.
- Yang, B., P. Ma, J. Shu, P. Zhang, J. Huang, and H. Zhang. 2018. Formation mechanism of secondary organic aerosol from ozonolysis of gasoline vehicle exhaust. *Environ. Pollut.* 234 :960–968. doi:10.1016/j.envpol.2017.12.048.